Title: The Geology and Geophysics of Kuiper Belt Object (486958) 2014 MU69

Authors: J.R. Spencer[1]*, S.A. Stern[1], J.M Moore[2], H.A. Weaver[3], K.N. Singer[1], C.B Olkin[1], A.J. Verbiscer[4], W.B. McKinnon[5], J.Wm. Parker[1], R.A. Beyer[6,2], J.T. Keane[7], T.R. Lauer[8], S.B. Porter[1], O.L. White[2], B.J. Buratti[9], M.R. El-Maarry[10], C.M. Lisse[3], A.H. Parker[1], H.B. Throop[11], S.J. Robbins[1], O.M. Umurhan[2], R.P. Binzel[12], D.T. Britt[13], M.W. Buie[1], A.F. Cheng[3], D.P. Cruikshank[2], H.A. Elliott[14], G.R. Gladstone[14], W.M. Grundy[15], M.E. Hill[3], M. Horanyi[16], D.E. Jennings[17], J.J. Kavelaars[18], I.R. Linscott[19], D.J. McComas[20], R.L. McNutt Jr.[3], S. Protopapa[1], D.C. Reuter[17], P.M. Schenk[21], M.R. Showalter[6] , L.A. Young[1], A.M. Zangari[1], A.Y. Abedin[18], C.B. Beddingfield[6], S.D. Benecchi[11], E. Bernardoni[16], C.J. Bierson[23], D. Borncamp[24], V.J. Bray[25], A.L. Chaikin[26], R.D. Dhingra[27], C. Fuentes[28], T. Fuse[29], P.L Gay[11], S.D.J. Gwyn[18], D.P. Hamilton[30], J.D. Hofgartner[9], M.J. Holman[31], A.D. Howard[32], C.J.A. Howett[1], H. Karoji[33], D.E. Kaufmann[1], M. Kinczyk[34], B.H. May[35], M. Mountain[36], M. Pätzold[37], J.M. Petit[38], M.R. Piquette[16], I.N. Reid[39], H.J. Reitsema[40], K.D. Runyon[3], S.S. Sheppard[41], J.A. Stansberry[36], T. Stryk[42], P. Tanga[43], D.J. Tholen[44], D.E. Trilling[45], L.H. Wasserman[15]

Affiliations:

[1] Southwest Research Institute, Boulder, CO 80302, USA

[2] NASA Ames Research Center, Moffett Field, CA 94035-1000, USA

[3] Johns Hopkins University Applied Physics Laboratory, Laurel, MD 20723, USA

[4] Department of Astronomy, University of Virginia, Charlottesville, VA 22904, USA

[5] Department of Earth and Planetary Sciences and McDonnell Center for the Space Sciences, Washington University, St. Louis, MO 63130, USA

[6] SETI Institute, Mountain View, CA 94043, USA

[7] Division of Geological and Planetary Sciences, California Institute of Technology, Pasadena, CA 91125, USA

[8] National Optical Astronomy Observatory, Tucson, AZ 26732, USA

[9] Jet Propulsion Laboratory, California Institute of Technology Pasadena, CA 91109, USA

[10] Department of Earth and Planetary Sciences, Birkbeck, University of London WC1E 7HX, London, UK

[11] Independent Consultant, Washington, D.C.

[12] Massachusetts Institute of Technology, Cambridge, MA 02139, USA

[13] Department of Physics, University of Central Florida, Orlando, FL 32816, USA

[14] Southwest Research Institute, San Antonio, TX 78238, USA

[15] Lowell Observatory, Flagstaff, AZ 86001, USA

[16] Laboratory for Atmospheric and Space Physics, University of Colorado, Boulder, CO 80303, USA

[17] NASA Goddard Space Flight Center, Greenbelt MD, USA 20771

[18] National Research Council of Canada, Victoria, BC V9E 2E7, Canada

[19] Independent Consultant, Mountain View, CA 94043, USA

[20] Department of Astrophysical Sciences, Princeton University, Princeton, NJ 08544, USA

[21] Lunar and Planetary Institute, Houston, TX 77058, USA

[22] Earth and Planetary Science Department, University of California, Santa Cruz, CA 95064, USA

[23] Earth and Planetary Science Department, University of California, Santa Cruz, CA 95064, USA

[24] Decipher Technology Studios, Alexandria, VA 22314

[25] Lunar and Planetary Laboratory, University of Arizona, Tucson, AZ 85721, USA

[26] Independent Science Writer, Arlington, VT 05250, USA

[27] University of Idaho, Moscow, ID 83844, USA

[28] Departamento de Astronomía, Universidad de Chile, Santiago, Chile

[29] Kashima Space Technology Center, National Institute of Information and Communications Technology, Kashima, Ibaraki 314-8501, Japan

[30] Department of Astronomy, University of Maryland, College Park, MD 20742, USA

[31] Center for Astrophysics, Harvard-Smithsonian Center for Astrophysics, Cambridge, MA 02138, USA

[32] Department of Environmental Sciences, University of Virginia, Charlottesville, VA 22904, USA+D132

[33] National Institutes of Natural Sciences, Tokyo, Japan

[34] Marine, Earth, and Atmospheric Sciences, North Carolina State University, Raleigh, NC 27695, USA

[35] Independent Collaborator, Windlesham, England, GU20 6YW, UK

[36] Association of Universities for Research in Astronomy, Washington, DC 20004, USA

[37] Rheinisches Institut für Umweltforschung an der Universität zu Köln, Cologne 50931, Germany

[38] Institut UTINAM, UMR 6213, CNRS, Universite Bourgogne Franche Comte, F-25000 Besancon, France

[39] Space Telescope Science Institute, Baltimore, MD 21218, USA

[40] Independent Consultant, Holland, MI 49424, USA

[41] Department of Terrestrial Magnetism, Carnegie Institution for Science, Washington, DC 20015, USA

[42] Roane State Community College, Oak Ridge, TN 37830, USA

[43] Université Côte d'Azur, OCA, Laboratoire Lagrange/CNRS UMR7293, 06304 Nice Cedex 4, France

[44] Institute for Astronomy, University of Hawaii, Honolulu, HI 96822, USA

[45] Department of Astronomy and Planetary Science, Northern Arizona University, Flagstaff, AZ, 86011, USA

*Correspondence to: spencer@boulder.swri.edu.

Revised August 27th 2019

Abstract: The Cold Classical Kuiper Belt, a swarm of small bodies in undisturbed orbits beyond Neptune, are the most primitive known objects in the solar system. The New Horizons spacecraft has provided our first close look at one of these objects, the contact binary 2014 MU_{69}. Continued data return from the spacecraft's January 1st 2019 flyby has revealed a remarkably smooth, lightly cratered, surface fundamentally different from that of previously visited solar system bodies, and likely dating from the end of the era of planetary accretion. The poles and equators of the two lobes of the contact binary are remarkably closely aligned, strongly constraining accretion mechanisms. MU69 has no detectable rings, and no satellites larger than 180 meters diameter within a radius of 8000 km.

One Sentence Summary: The New Horizons flyby of a primitive Kuiper Belt Object illuminates the era of planetary formation.

Main Text:

At 05:33:22 UT on January 1st 2019, the New Horizons spacecraft passed 3538 km from Kuiper Belt object (KBO) (486958) 2014 MU_{69}, nicknamed "Ultima Thule", henceforth "MU_{69}" (*1*). MU_{69} is a contact binary consisting of two distinct lobes, nicknamed Ultima (the larger) and Thule (the smaller), connected by a relatively narrow neck. Based on its semi-major axis, low orbital eccentricity and inclination (*2*), and its albedo and color (*1,2,3*), MU_{69} is almost certainly a member of the dynamically cold, non-resonant "cold classical" (CCKBO) population of Kuiper Belt objects, and probably a member of the tight orbital clustering of CCKBOs known as the "kernel" (*4*). Because there is no known mechanism for transporting objects onto these nearly circular orbits after their formation, and because of the low impact rates (*5*) and low temperatures in the Kuiper Belt, CCKBOs are thought to be the most dynamically and physically primitive known population of small bodies in the solar system. MU_{69}'s equivalent spherical diameter of 18 km (below), makes it about 8.5x smaller in diameter than the transition between the steep size-frequency distribution of larger CCKBOs and the shallower distribution of smaller CCKBOs at diameter ~100 km (*6*), and thus has the potential to shed light on the nature of this transition.

Since the submission of initial results from this flyby (*1*), additional flyby data have been downlinked, including: (i) the highest-resolution images, taken with the narrow-angle Long-Range Reconnaissance Imager (LORRI) camera (*7*). The LORRI images have 4x finer pixel scale (33 m/pixel) than the previous best 130 m/pixel Multicolor Visible Imaging Camera (MVIC) (*8*) images described in (*1*), though due to smear and relatively low signal-to-noise ratio (SNR), their effective resolution is only about 2x better than the MVIC images; (ii) many

additional LORRI images from earlier approach epochs, providing much improved SNR; (iii) improved LORRI distant approach rotational coverage, which improves shape and rotational parameters; and (iv) additional satellite and ring search data from LORRI and MVIC. This paper describes the improved knowledge of MU_{69}'s shape, geological evolution, and satellite and ring constraints resulting from these additional data, and from continued analysis of all data in hand.

Stereo Imaging

The improved resolution and SNR of the new data, particularly the pair of LORRI images designated CA04 and CA06 (Fig. 1A, Table S1) provides greatly improved stereo imaging to constrain the shape and topography of the close approach hemispheres of the two components. A stereographic terrain model derived from these images, as described in the Supplementary Materials and included there (Shape Model S1), is shown in Fig. 2. Typical relief in the stereo model on both lobes away from the neck region is ~0.5 km or less, roughly consistent with the 1.0 km and 0.5 km relief seen in limb profiles on Ultima and Thule respectively (*1*). Direct viewing of the stereo pair (Fig. 1A) provides additional topographic detail that is visible to the eye but is just below the resolution in the terrain model, and some of the interpretation in the geology section below is based on this subjective stereo.

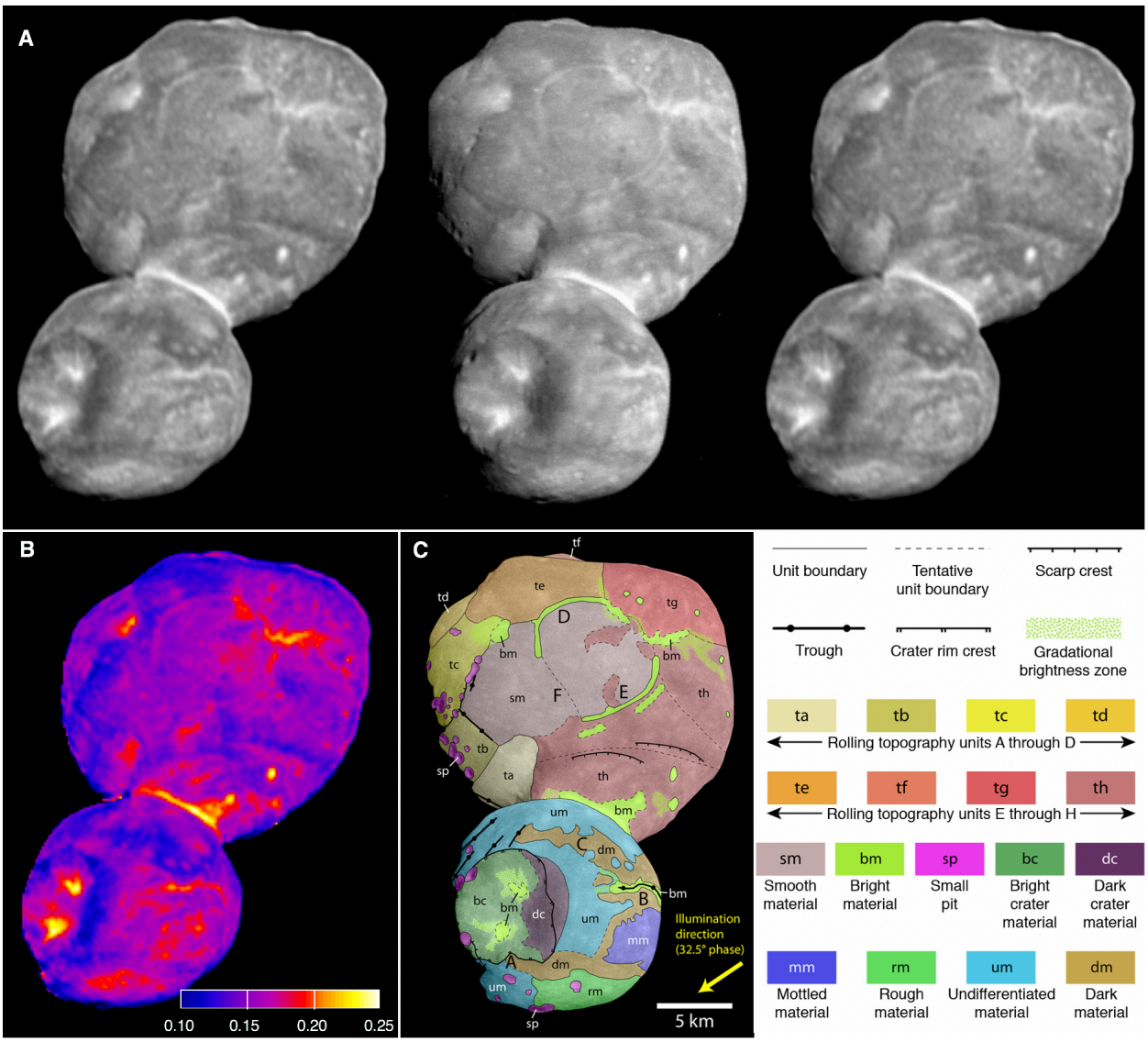

***Fig. 1**. Mapping of MU69. A. Cross-eyed (left+center) and direct (center+right) stereo pair image of 2014 MU69, taken by LORRI. The "Ultima" lobe is at the top and the "Thule" lobe is at the bottom (all names used here are informal). Left and right images: CA04, range = 27,860 km, phase = 12.9°, 138 m/pixel. Center image: CA06, range = 6,650 km, phase = 32.5°, 33 m/pixel. Both images have been deconvolved to remove the LORRI point-spread function, and motion blur in the case of CA06, to maximize detail. B. 0.6 μm normal reflectance map of MU69, based on image CA04. C. Geomorphological map of MU69. The base map is the deconvolved CA06 image. The positive (using the right-hand-rule) spin axis of MU69 is pointing approximately into the page. Capitalized letters identify locations mentioned in the text. The present mapping is physiographic in nature and is not intended to rigorously convey stratigraphic relations between units.*

Rotation and Global Shape Modeling

No periodic brightness variation (lightcurve) due to rotation was detected before encounter, with an upper limit amplitude of about 0.15 magnitudes (*9*). July 2017 and August 2018 stellar

occultations showed that MU$_{69}$ had an elongated, possibly contact-binary shape (*10*). The elongated shape and the low lightcurve amplitude implied that MU$_{69}$'s rotational pole was probably roughly aligned to the sun and the spacecraft's approach direction.

MU$_{69}$'s rotation and global shape are largely constrained by LORRI images taken between 2.2 days before the encounter, when MU$_{69}$ first exceeded 2 pixels in length, and 9 minutes after encounter, when MU$_{69}$ was last seen at high phase as a receding crescent. Disk-integrated photometry from earlier unresolved images was unable to detect the rotational lightcurve due to its low amplitude and confusion from the dense stellar background. The bulk of the shape information comes from a series of approach images with cadence between 1 hour and 20 minutes, starting 13.6 hours before closest approach, when MU$_{69}$ subtended 10 pixels in length (Fig. 3). These images covered 85% of the final 15.92-hour rotation, though only one hemisphere of MU$_{69}$ was well imaged because the rotational pole (below) was relatively close to both the direction of the sun and New Horizons' approach direction.

Using the same techniques described in (*1*), but incorporating the additional rotational coverage images now available, the rotational period of MU$_{69}$ is unchanged at 15.92 ± 0.02 hours, but its positive rotational pole pointing is refined to Right Ascension = 317.5 ± 1°, Declination = -24.9 ± 1° in the J2000 equatorial frame. This rotation rate is typical of other cold classical KBOs (*11,12,13*). The resulting obliquity of MU$_{69}$'s pole to its orbit is 99.3°, and the rotational pole is 39.4° from the New Horizons approach vector and 28.1° from the direction of the Sun during the encounter. The shape model predicts a lightcurve peak-to-peak amplitude of 0.05 magnitudes as seen from New Horizons' approach direction, consistent with the earlier non-detection of the lightcurve.

The low-resolution global shape model (Shape Model S2, Supplementary Materials) used all available observations—even the early, distant observations—to refine the model. In particular, the CA07 observation (Fig. 4, Table S1) of the illuminated double-crescent of MU$_{69}$, provides a constraint on how thick the unilluminated +Z side can be, based on which stars are and are not eclipsed by the object (Fig. 3). It is clear from Fig. 3 that the shape model is still not perfect: for instance, compared to the model, the images show a more open neck and flatter distal end of Thule between 12/31 21:38 and 1/1 01:12.

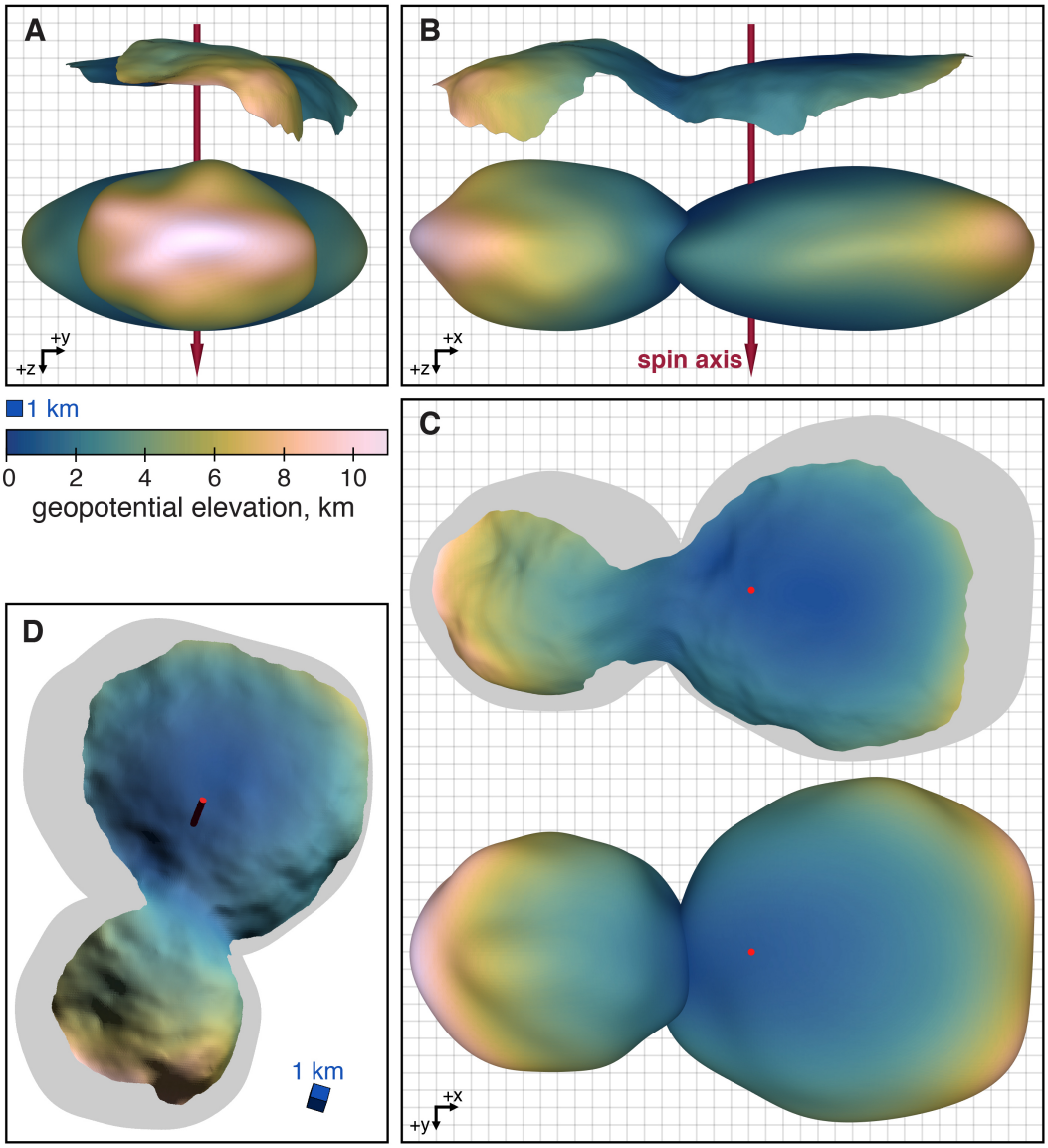

Fig. 2. *Stereo and global shape models. A – C: Comparison of the stereo shape model of the encounter face (top of each panel) to the global shape model (bottom of each panel), as seen from the -X (Thule) direction (A), the +Y direction (B), and the south polar (-Z) direction (C). The +Z ("North") axis is the positive direction of the spin axis, according to the right-hand rule. Each model is colored to show the variation in geopotential across the surface. The stereo model has been trimmed to remove edge effects. D: Stereo model seen from the CA06 viewing geometry (Fig. 1A, right), but with different lighting, chosen to highlight the small-scale topography.*

The best-fit global shape of the object is two roughly ellipsoidal lobes with overall dimensions of 36 x 20 x 10 km. Maximum dimensions of Ultima, and Thule, are 20.6 x 19.9 x 9.4 km and 15.4 x 13.8 x 9.8 km respectively. The uncertainty for these dimensions is roughly 0.5 x 0.5 x 2.0 km in X, Y, and Z respectively: uncertainty is larger in the Z direction because the flyby imaged little of the +Z (northern) half of the object. The total volume is 3210 ± 650 km^3, equal to a

sphere of diameter 18.3 ± 1.2 km. This volume is 30% larger than the previous estimate of 2450 km^3 (*1*), though consistent within uncertainties. The larger lobe has a volume equal to a sphere of diameter 15.9 ± 1.0 km, while the equivalent diameter for the smaller lobe is 12.9 ± 0.8 km. These values give a volume ratio (and mass ratio if densities are equal) of 1.9 ± 0.5.

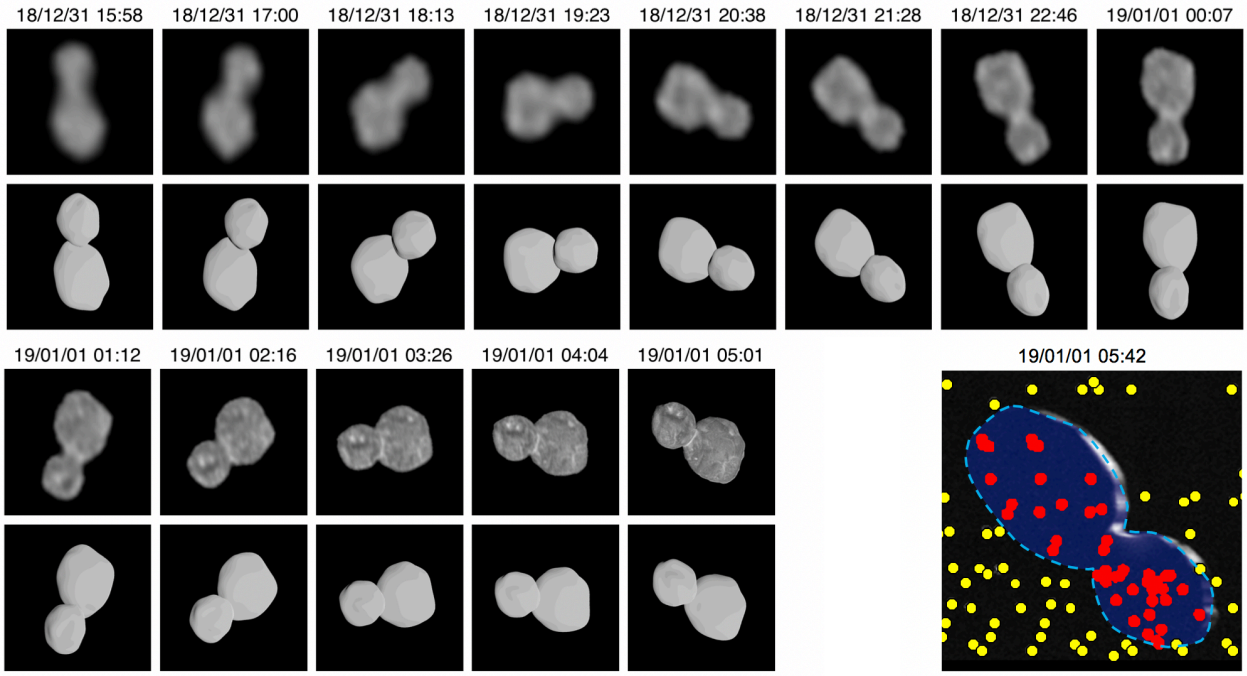

Fig. 3. *Shape model compared to LORRI images. Small frames: Selected deconvolved LORRI approach images of MU$_{69}$, compared to synthetic images with the same geometry derived from the global shape model. Images have been scaled to a constant frame size of 44 x 44 km, so that the images become sharper as time progresses and range decreases. Celestial north is up. Larger frame: the CA07 departure image, with the silhouette (dark blue) and outline (light blue, dashed) of the shape model superposed. Red and yellow dots indicate the locations of occulted and unocculted stars respectively in the 6-frame CA07 sequence, used to constrain the shape of the unilluminated hemisphere.*

Fig. 2 compares the global shape model to the stereo model of the encounter (-Z) face of MU$_{69}$. There is broad agreement between the two techniques, though the south polar region of Ultima is flatter in the stereo model, and the neck is smoother (a slope discontinuity at the neck is an intrinsic feature of the global shape model, due to its dual-lobe nature). We expect the stereo model to be more reliable than the global shape model in the south polar and neck regions, because of the additional information that is incorporated into the stereo model due to the matching of albedo features, and the fact that albedo features can produce artifacts in the global shape model, which assumes uniform surface albedo. However, near the limbs the stereo model performs poorly because foreshortening makes feature matching difficult, while the global shape model is strongly constrained.

Fig. 4. *MU_{69} seen at high phase. New Horizons' last view of MU_{69} (CA07), taken with the LORRI camera 9.4 minutes after closest approach at phase angle 152°, range 8,800 km, and resolution 175 m/pixel. This image has been deconvolved to remove the motion smear visible in the version in the larger lower-right panel of Fig. 3. The Ultima lobe is in the upper left and the Thule lobe is in the lower right.*

Gravity Modeling

The irregular shape of MU_{69} yields an unusual geophysical environment. To probe this, we calculated MU_{69}'s geopotential (the sum of the gravitational and rotational potentials in a body-fixed reference frame) using the low-resolution shape model, the 15.92-hour rotation period, and an assumed bulk density. In the absence of gravity measurements or detected satellites, the density of MU_{69} is not directly constrained. However, if the neck of MU_{69} is assumed to have no tensile strength, the density must be >290 kg/m^3, or the rotation would overcome the mutual gravity of the two lobes, causing them to separate. We assume a nominal bulk density of 500 kg/m^3 similar to the observed densities of cometary nuclei (e.g. (*14*) for comet 67P/Churyumov-Gerasimenko), resulting in mean surface gravity of ~1 mm/s^2. If this density is correct, the fact that the two lobes can support each other across their ~28 km^2 contact area implies a compressive strength, accounting for centrifugal force, of greater than 2.3 kPa.

Figure 2 also shows the geopotential altitude across MU_{69}. The geopotential altitude is calculated by dividing the total accelerations by the geopotential, and represents elevation with respect to an equipotential (*15*). The geopotential is calculated from the global shape model, and is evaluated on the surfaces of the global shape model, and also on the stereo model with position matched to the global shape model as described in the Supplementary Materials. This approach results in slight inaccuracies in the geopotential calculated across the stereo model—as there are regions where the stereo model rises above/below the surface of the global shape model. We focus on general trends that are robust to the current uncertainties in the shape model. The geopotential is

highest at the distal ends and equator, and decreases with increasing latitude on each lobe, reaching a global minimum in the neck. Surface slopes (derivatives of the geopotential (*15*)) are generally gentle (<20°) and slope downward to higher latitudes and into the neck region (Fig. S1). If material can flow downslope, then it will collect at higher latitudes and in the neck region. The stereo model reveals that the neck is relatively smooth, with shallow slopes. The global shape model shows slopes of >30° at the neck, but this steepness is in part an artifact of the global model's treatment of MU_{69} as two separate overlapping bodies.

The configuration of the two lobes of MU_{69} provides important clues its formation and evolution (*1,16*). Using the same assumptions as above, we calculate the principal axes of inertia for Ultima and Thule by slicing MU_{69}'s neck at the narrowest point. The new shape model confirms that the maximum axis of inertia of Ultima is aligned within < 5º to its Thule counterpart, and the equatorial plane of the two bodies is also almost coincident in space, with the estimated center of mass of Thule displaced only 0.18 km from the equatorial plane of Ultima.

Surface Units

We have generated a new map of 0.6 μm normal reflectance (defined as the specific intensity (I/F) when the incident and emission angle are both 0°) (Fig. 1B). The map is derived from the high-SNR CA04 image, using a merger of the global and stereo shape models to determine illumination at each point, and a lunar-like photometric function (*17*). Assuming this photometric function, which exhibits no limb darkening at zero phase, the normal reflectance is equal to the geometric albedo of a body covered in material with that location's photometric properties. MU_{69}'s mean 0.6 μm normal reflectance is 0.15, roughly consistent with its overall 0.55 μm geometric albedo of 0.165 (*1*).

The new images of MU_{69} have enabled a new geological unit map of MU_{69} that supersedes the preliminary map in (*1*) (Fig. 1C). See the Supplementary Materials for a discussion of mapping units and techniques. Thule and Ultima have distinctly different surface appearances and thus different mapped surface units, and are described separately below. Mean and standard deviation of the normal reflectance is 0.150 and 0.023 respectively for Ultima, and 0.149 and 0.028 respectively for Thule: the larger standard deviation on Thule reflects its distinct appearance.

Thule: Thule is distinct in appearance from Ultima (Fig. 1A, B). As noted in (*1*), Thule is dominated by a large depression (informally named Maryland), which is very likely to be an impact crater. The projected crater rim measures ~6.7 by 6 km across in the image plane, with the longer axis roughly aligned with the principal axis of MU_{69}. The ellipticity may be due to foreshortening, in which case Maryland may be circular with diameter 6.7 km. Stereo measurements show that the location of the deepest well-determined point in Maryland is 0.51 km below a plane defined by the rim, or 1.3 km below the surface of a sphere with Thule's mean radius, giving a depth/diameter ratio of 0.08 – 0.19. This depth/diameter ratio is comparable to those on other bodies with gravities similar to MU_{69}'s ~1 mm s^{-2}, including asteroids Šteins (~0.12, 0.8-1.3 mm s^{-2}, (*18*)) and Eros (~0.13, 2.4-5.5 mm s^{-2}, (*19*)), though these bodies are composed of different materials and may have different porosities. Stereo imaging (Fig. 1A) reveals that the part of its rim furthest from Ultima features an unusual promontory of the "*dm*" unit protruding into the crater (A in Fig 1C), at an elevation similar to the rest of the rim.

Albedo patterns across Thule are complex. There are two patches of bright material (unit *bm*) within Maryland, which show discrete boundaries near the crater bottom, and feather towards the

crater rim. Straddling the Maryland rim on the side opposite the bright patches is discrete, dark crater rim material (unit *dc*), which contrasts with the brighter terrain (unit *bc*) that forms the remainder of the crater interior. Elsewhere on Thule, discrete morphological units exhibit almost twofold albedo variations (Fig. 1B). The rough terrain unit (*rm*), found at the distal end of Thule, forms a relatively flat facet, brighter than its immediate surroundings. The low sun angle on this facet reveals a rough surface texture at a scale of a few hundred meters apparently mostly composed of sub-km pits, with one prominent ~150 m diameter pit (27 in Fig. 6A) which resembles a small, fresh, bowl-shaped impact crater. Another nearby mottled bright unit (*mm*), may be similar, but is seen at a higher sun angle so topographic roughness is not apparent, and has a distinctly crenulated and angular margin relative to that of unit *rm* (B in Fig. 1C).

Dark material surrounding the *mm* material seems to be part of a unit (*dm*) that wraps around much of the remainder of the observable surface of Thule- this material is the darkest on MU_{69}, with minimum 0.6 μm reflectance of 0.11. In places (C in Fig. 1C), it has a boundary with pointed and angular protrusions and rounded indentations, which may be evidence for material erosion and removal due to scarp retreat (*1*). Near C in Fig. 1C, there are also bright circular patches within the dark material. Running down the center of the principal mapped outcrop of dark material is a sinuous unit of bright material, which appears in stereo observations to occupy a V-shaped trough. The rest of the surface of Thule is nondescript at the available lighting and resolution and has been mapped as undifferentiated material (unit *um*). Crossing the undifferentiated material near the terminator between Maryland and Ultima, however, are a series of sub-parallel troughs, which are reminiscent of structural troughs seen on other comparable-sized bodies, for instance asteroid Eros (*20,21*), Saturn satellites Epimetheus and Pandora (*22*), and the Martian satellite Phobos (*23*).

The new data confirm that the bright "neck" region connecting Ultima and Thule has a diffuse margin at least on the Ultima side, but extreme foreshortening makes it difficult to characterize its margin on the Thule side.

Ultima: The larger lobe, Ultima, is very different in appearance from Thule. (*1*) mapped Ultima as being composed of a series of roughly same-sized, discretely bounded, rolling topographic units, though Fig. 1C interprets some of these units and their boundaries differently, as described below. The new data confirm the discrete nature of many of the units (*ta* through *tg*). Those near the terminator, *ta – td*, are distinctive, being relatively bright (Fig. 1B) (though *ta* is noticeably less red than the others (*3*)), and clearly separated from the rest of Ultima by a common, continuous scarp or trough, as noted above. Units *tg* and *th* appear more mottled than adjacent units, and stereo imaging of these suggests that their surface consists of dark ridges and hills surrounding brighter low terrain.

The rest of Ultima is occupied by smooth material (unit *sm*) of moderate albedo, transected by a series of distinctive bright linear features (unit *bm*), some of which form an incomplete annulus. In some areas (D in Fig. 1C) the inner margin of the annulus appears sharply bounded, possibly with an outward-facing scarp. In this and other places within unit th (and possibly te), the annulus shows an apparent concentric structure, with the outer, concentric portions appearing more gradational with the surrounding terrain than the main inner portion. Stereo observations (Figs. 1A, 2D) show that terrain within the annulus is relatively flat compared to the undulating nature of the rest of the visible portion of Ultima, and suggest that the annulus occupies a shallow trough. At the base of unit *tg*, the annulus appears to coincide with diffuse bright material which appears to interrupt the annulus and so may be superimposed upon it. In two

places, what appear to be dark hills extend into the *sm* unit. In one case (E in Fig. 1C) these hills seem to be an extension, cut by the *bm* annulus, of similar hills on unit *th*. We discuss the possible origin of the annulus and similar features below.

Geological Interpretation

Across MU_{69}, the new data, in particular the improved stereo, confirm that relatively bright material on both Ultima and Thule occurs preferentially in depressions. The brightest material on Ultima (the possible crater number 17 on Fig 6A), on Thule (the bright possible craters 42 and 43 in Fig. 6A), and in the bright collar between the two lobes all have the same normal 0.6 μm reflectance, 0.24, suggesting that the bright material has similar chemical and physical properties everywhere. The most extensive bright region, found in the topographic low of the "neck" region, may be simply the most extreme example of a process that occurs more generally to brighten low-lying material across MU_{69}. The stereo data thus support the hypothesis of (*1*) that loose, poorly consolidated, likely fine-grained bright material moves downslope and accumulates in depressions, which would imply that bright material is more mobile than dark material on MU_{69}. The complex albedo patterns on Thule, and their crenulated margins, may result from the exposure and differential erosion of multiple lighter and darker layers oriented roughly parallel to its surface, though independent topographic information is of insufficient quality to confirm this explanation.

(*1*) proposed one alternative that Ultima is composed of smaller sub-units that accreted separately. However, the improved imagery and topography raise questions about this interpretation. First, the central *bm* annulus, enclosing what was mapped as a discrete sub-unit in (*1*) appears to be a relatively young feature, and not an unmodified primordial boundary, for the following reasons: (i) the annulus is incomplete, with no discernable topographic feature or textural change in the gap region where it is missing (F in Fig 1C)- for this reason we map a continuous unit, *sm*, across this gap; (ii) even where the annulus is conspicuous, it cuts across flat terrain for most of its length; and (iii) dark hills of the *mh* sub-unit appear to form a continuous physiographic unit cut by the annulus at E, Fig 1C, and (iv) the partially concentric nature of the annulus suggests a structural basis, not significantly obscured by subsequent deposition. Secondly, though other proposed sub-units are distinguishable by differing surface textures, albedos and modest topographic inflections or other surface features, the overall shape of Ultima is smooth and undulating, without major topographic discontinuities like that between Ultima and Thule, as would be expected from accretion of large pre-existing sub-units. Erosion and alteration over the past 4.5 Ga is likely to have modified the optical surface and the uppermost upper few meters (*24*) but probably does not explain the smoothness seen at the > 30 meter scale of the New Horizons imaging resolution.

Some possible explanations for the appearance of the annulus and other sub-unit boundaries are illustrated in Fig. 5. The sub-units may have been soft enough at the time of merger that they conformed to each other's shapes on contact (*25,1*) (Fig 5A), though no evidence for impact deformation is seen. In order for such deformation to take place at the time, the shear strength of the merging components must have been no more than 2 kPa as this is the ram pressure of an impacting body assuming a merger velocity of 1-2 m s^{-1} and a material density of 500 kg m^{-3}. The possibility that they flowed viscously due to gravity after contact while still soft (Fig. 5B) can be discounted, because such flow would require an implausibly low shear strength of ~100 Pa. Mass-wasting may have filled in original gaps between the sub-units while preserving a sharp boundary between them (Fig. 5C), though except in the case of the boundary of *tg* noted

previously, the absence of obvious boundaries between material transported by mass wasting, and in-situ material argues against this as a general explanation. The fact that mass wasting has not significantly filled the much larger depression between Ultima and Thule also implies that any major mass wasting process must have ceased before the merger of the two objects. The original discontinuities may have been buried by subsequent accretion or redistribution of surface material (Fig. 5D). The boundaries would then need to be re-activated in some way in order to still be visible on the surface, possibly by collapse into subsurface voids or degassing of super-volatiles, which may explain the trough-like appearance of parts of the *bm* annulus, and the troughs and pits seen at low sun between the *ta – td* sub-units and the rest of Ultima. However, it's not clear how the burial would preserve different surface textures for the different sub-units. Alternatively, Ultima may be monolithic, and the visible boundaries may be secondary (Fig. 5E), produced for instance by subsequent fracturing. For the annulus, we consider the evidence to be most consistent with scenarios D and E in Fig. 5. However, in any of these cases, the processes that produced the distinctive surface textural contrasts between the units, in particular the patches of dark hills and ridges, is unknown.

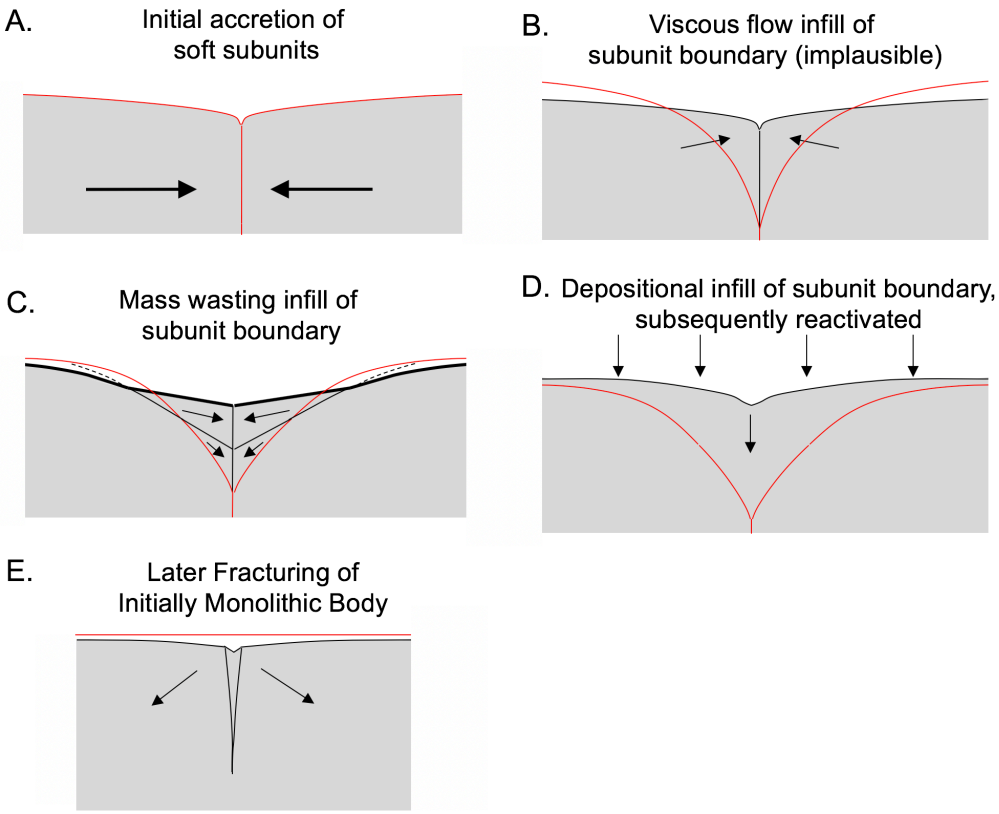

Fig. 5. *Illustration of possible explanations for the appearance of the boundaries between terrain subunits on Ultima. Original surface shown in red. See text for discussion.*

Pits and Craters

In addition to the 7 km diameter probable impact crater Maryland, scattered across the body of Ultima are numerous roughly circular sub-km bright patches and pits, though even if these are mostly impact craters the crater density is relatively light compared to many other small bodies

(*1*). The bright patches are generally seen in high-Sun areas away from the terminator, and some of these patches appear to occupy depressions in stereo pairs. These may be equivalent to the pits seen in low-Sun areas near the terminator (unit *sp*, Fig.1C), and it is possible that the near-terminator pits also feature bright material on their floors that is invisible due to unfavorable lighting.

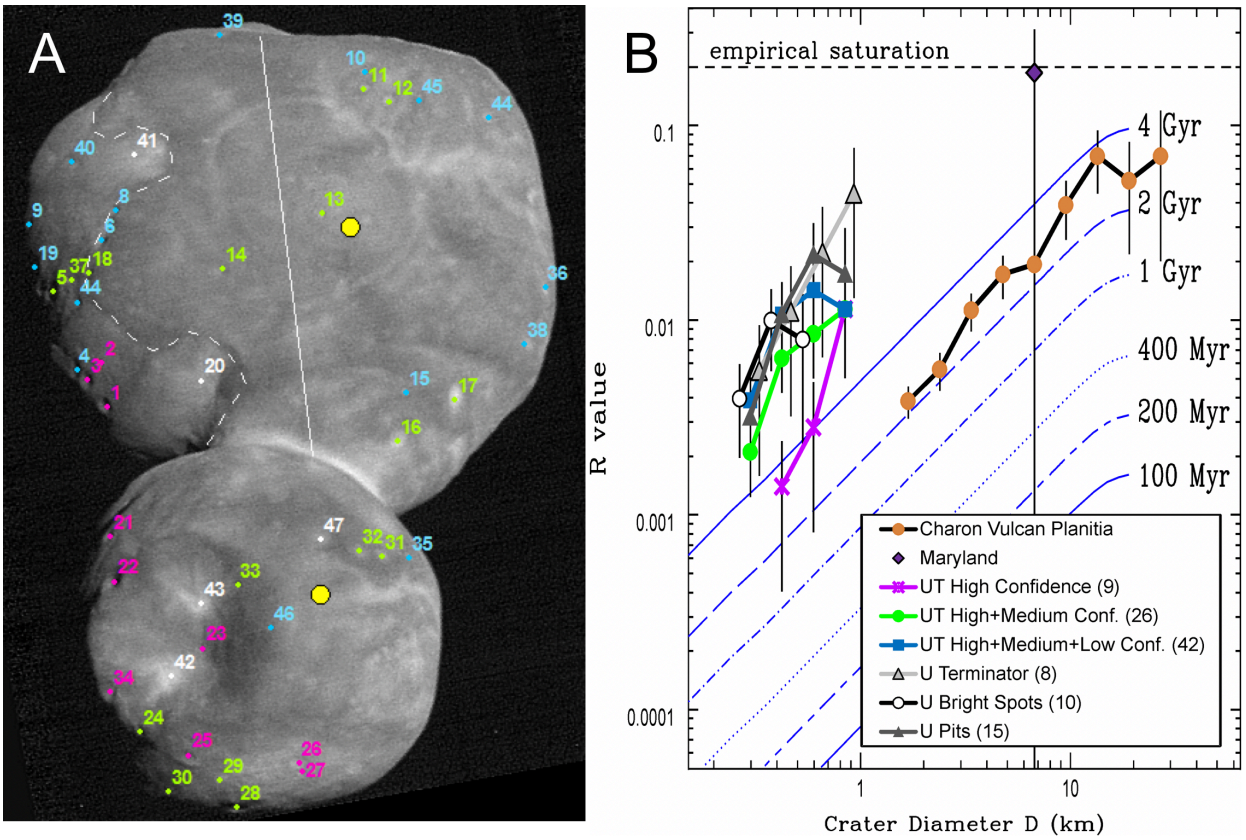

Fig. 6. *Craters and Pits on MU$_{69}$. A. Locations of features considered for crater analysis: numbers refer to crater listings in Supplementary Data Table S1. Color denotes confidence class: magenta = high confidence, green = medium confidence, cyan = low confidence. Features indicated in white are considered to be highly unlikely to be of impact origin and are not included in the crater statistics. The solid white line indicates the split of the Ultima lobe into a low-sun half with more visible depressions (the "U_Pits" region, left) and a high-sun half with bright spots (the "U_Bright" region, right). The white dashed curve delineates combined geologic units ta, td, tc, and td, designated "U_Term", considered together for crater density determination. The yellow dots indicate the planetocentric subsolar point on each lobe according to the shape model. B. The size-frequency distribution of craters on MU$_{69}$ is shown per crater subgroup and region described in the text, Fig. 6a, and Supplementary Materials. Note that in this panel, the green curve includes both high and medium confidence classes, and the blue curve includes all confidence classes. Parenthetical numbers are the total number of craters/pits in each category. The MU$_{69}$ crater data are compared to crater densities on Charon's Vulcan Planitia (VP), from (35) without diameter adjustments for gravity or velocity scaling, and to predictions based on an impactor flux model for six different ages of surfaces on MU$_{69}$ and gravity regime scaling (blue curves;(5)). The U_Term and U_Bright distributions are*

offset in horizontally by a small amount for clarity. The empirical saturation line refers to a traditional D^{-3} differential power law distribution (62).

We have now categorized these bright patches and pits to reflect our confidence that they are impact craters based on the morphology expected for either fresh or degraded impact craters (see Supplementary Materials, and the listing of craters in Data Table S1), as determined by multiple independent mappers. The spatial arrangement of the potential craters and their relationship to other geologic features was one of the criteria used. For instance, at noted above, a chain of pits that is coincident with a scarp on the boundary between units *tc* and *sm* possibly originated via surface collapse rather than impact (*1*). For a fresh crater formed on a relatively flat and smooth surface, a crater rim is expected to be close to circular and raised above the surrounding terrain (unless the terrain is substantially porous (*26*), though image resolution does not always permit identification of the raised rim. Also, the shape of the interior of the crater is expected to be bowl-like with a depth/diameter ratio typically not higher than ~0.2 (*27*). The predicted modal impact velocity onto MU_{69} is ~300 m s^{-1} (*5*), which is sufficient to form craters with typical morphologies (see discussion in the Supplementary Materials). In the case of MU_{69}, the few lowest velocity impacts (under a few tens of m/s) are unlikely to leave conspicuous depressions, but these impacts are a small fraction of the total (*5*).

The formation of a crater on a slope or modification by later geologic processes (such as mass wasting or a subsequent fault near the crater) may also alter the crater's appearance. These smaller features were subdivided in three ways (see Fig. 6A, and the Supplementary Materials for details): (i) all pits and bright patches were subdivided based on our confidence that they are impact craters, (ii) features on Ultima were subdivided into pits nearer the terminator, and bright patches away from the terminator, separated by the solid white line in Fig. 6A, and (iii) a combination of geologic units ta, tb, tc, and td, designated "U_Term" (Fig. 6A), was analyzed separately, because the entire combined unit has low-angle lighting optimal for crater identification. These subdivisions yielded a range of plausible crater densities, shown in Fig. 6B as a crater relative- or R-plot (see Supplementary Materials for an explanation of R values). Overall R values for each dataset are somewhat uncertain as they depend on the areas used for each distribution and of course densities are lower if uncertain craters are excluded. But despite these uncertainties, the range of crater densities is less than a factor of 10 for a given diameter bin.

Besides Maryland, all of the other possible impact features are 1 km in diameter or smaller. While the large diameter gap between Maryland and second-largest crater on MU_{69} seems unusual, it does not obviously disfavor a single power-law size distribution for the craters. We test a model crater population with a power-law size distribution with a slope of $q = -2$ against the observed MU_{69} craters in the "UT_Medium" category, which includes high- and medium-confidence craters. The resulting Anderson-Darling statistic indicates no substantial disagreement between the model and observed sample, with a significance level of $p <= 17\%$.

Our analysis shows that MU_{69} appears to be only modestly cratered, relative to heavily cratered small objects like Phobos (Fig. S2), and there are some areas on MU_{69} where very few, if any, potential craters exist, in particular the part of Ultima between the dashed and solid white lines in Fig. 6A.

Surface age can be estimated from the observed crater density. The impact flux estimates on MU$_{69}$ have been converted to crater densities for several surface ages (*5)* in Fig. 6B. Age estimates are uncertain, given the uncertainty in identifying which craters are impact-generated, and because the model curves will shift based on the crater scaling parameters used. Strength-regime scaling as opposed to the gravity-regime scaling employed in (*5)* could in principle reduce the sizes of craters produced, if the surface strength of MU$_{69}$ were great enough. The expected strengths of porous cometary surfaces are, however, generally low enough (~1 kPa or less (*28*)) that the observed craters on MU$_{69}$ should have formed in the gravity regime. In contrast, accounting for the additional cratering in an early but brief dynamical instability phase in the outer solar system (*29*) would shift the model curves in Fig. 6B upward, although possibly by no more than a factor of two (*5*). Low relative densities of small craters are also observed on near-Earth asteroids, and are conventionally explained as due to seismic shaking from larger impacts or surface evolution due to changes in spin state (*30,31,32)*. MU$_{69}$'s spin state is likely to have evolved only very slowly (*16*), there do not appear to be sufficient impacts to act as effective seismic sources, and MU$_{69}$'s likely high porosity makes seismic energy propagation highly inefficient in any case. Overall, despite the paucity of craters on its surface, the observed crater density is consistent with a crater retention age of greater than ~4 billion years. The visible surface at the scale of the LORRI image resolution thus plausibly dates from the end of the accretionary period.

Though the diameters of observed craters on MU$_{69}$ (apart from Maryland) are smaller than those measured in the Pluto system, and the MU$_{69}$ datasets suffer from small number statistics, the slopes of the MU$_{69}$ and Pluto system craters are consistent. Using the Approximate Bayesian Computation forward-modeling methods (*33*, *34*), we estimate the posterior probability density functions for the parameters of independent truncated power-law crater size-frequency distribution models for 2014 MU$_{69}$'s and Charon's (*35*) observed crater populations (for craters < 10 km diameter, below the observed break in slope). We then conduct the same analysis for a model with a common slope q between the two populations, but a separate offset. The mean slope q = -1.8 $^{+0.4}_{-0.6}$ for Charon alone, q = -2.3$^{+0.6}_{-0.6}$ for 2014 MU$_{69}$ alone, and q = -2.0$^{+0.4}_{-0.3}$ for the joint set (95% confidence). However, as seen in Fig. 6B, crater density on MU$_{69}$ is higher than would be obtained from an extrapolation of the Charon slope and density to sub-km craters.

Satellites and Rings

Prior to the MU$_{69}$ flyby, constraints on the prevalence of satellites and rings around sub-100 km diameter Kuiper Belt objects were limited. Larger CCKBOs are frequently members of orbiting binary pairs (*36)*, but satellites with a primary/secondary brightness ratio larger than 20 have not been found for KBOs smaller than 500 km diameter (*37*), though this is likely partly due to observational biases. Satellites with high primary/secondary brightness ratio are however common around large KBOs in non-CCKBO populations. The presence or absence of satellites provides a constraint on formation of the MU$_{69}$ contact binary (for instance satellites provide one potential way to remove angular momentum from the central body). At least two known asteroid contact binaries have small satellites: the large Trojan Hektor has a satellite with orbital radius just 5x the primary radius and a diameter 5% that of the primary (*38*), and large bi-lobed main-belt asteroid Kleopatra has two known satellites orbiting at 8x and 12x the primary radius, with diameters 6% that of the primary (*39*).

New Horizons conducted a nested series of satellite searches with the LORRI camera during its approach to MU$_{69}$, using stacks of many images taken using 4x4 pixel binning to increase

sensitivity and reduce data volume. New search data returned since the submission of (*1*) has greatly improved the depth and breadth of the search results: see Supplementary Materials for details. No satellites have been found so far. We can exclude satellites larger than 100 – 180 meters in diameter (~0.5% the diameter of the primary) from MU_{69}'s surface out to 8000 km radius, and < 300 m diameter throughout most of the Hill sphere, assuming albedos similar to MU_{69} itself (Fig. 7). Satellites analogous to those of Hektor and Kleopatra can thus be excluded.

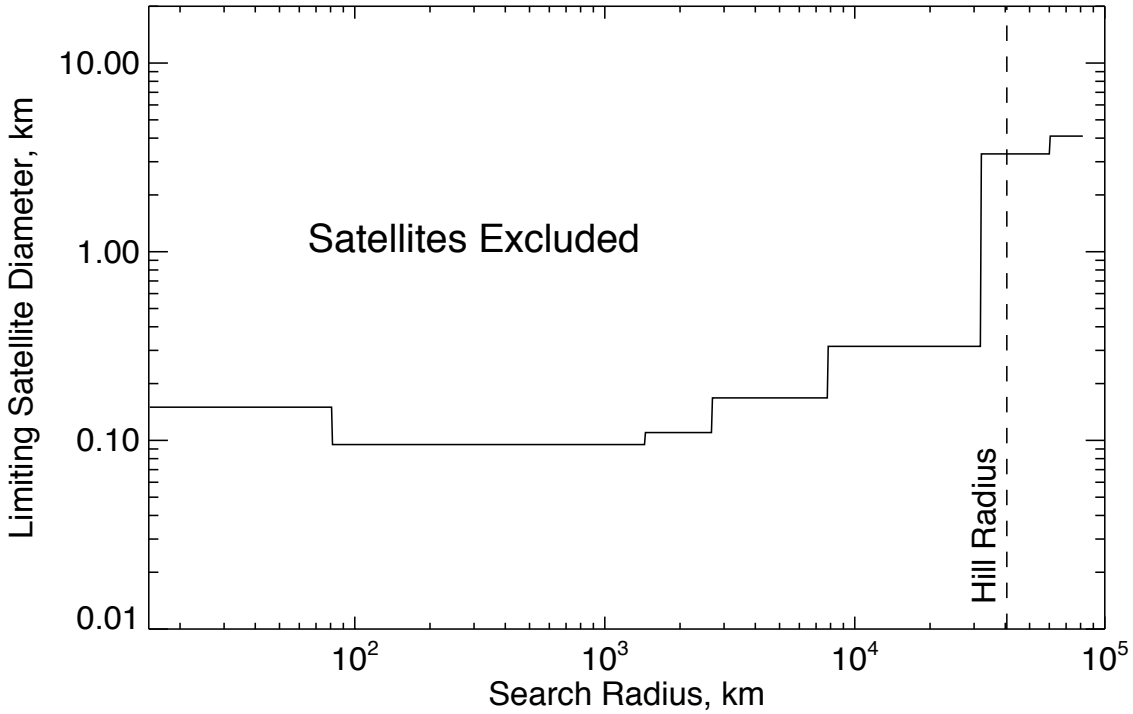

Fig. 7. *Upper limits to possible satellites of MU_{69} as a function of distance from the primary. Limits assume photometric properties similar to MU_{69} itself. The Hill radius assumes a density of 500 kg m^{-3}.*

The prevalence of rings around small KBOs was unknown, but the surprising discovery of rings around Chariklo (*40*), Haumea (*41*), and perhaps Chiron (*42*) raises the possibility of their existence around other distant small bodies. The New Horizons flyby provided an unprecedented opportunity to search for rings around a small KBO.

Searches for rings and dust clouds within the MU_{69} environment were performed at all phases of the encounter. The LORRI hazard and satellite searches on approach, discussed above, constrained backscattered light due to any ring or dust clouds to $I/F \lesssim 2 \times 10^{-7}$ at 11° phase for a 10-km-wide ring, assuming neutral colors (*1*), fainter than Jupiter's main ring ($I/F = 7 \times 10^{-7}$ at 11° phase). Dedicated searches, not reported in (*1*), were also conducted in forward-scattered light after closest approach, 1.7 – 2.3 hours after closest approach at a phase angle of 168°, covering radii up to 6,000 km from MU_{69}. The MVIC instrument, which has better rejection of scattered sunlight than LORRI, was used in its panchromatic framing mode, with total exposure times of 30 seconds. See (*43*) for reduction and analysis methodologies. No rings or dust

structures were seen, with an upper limit I/F of ~1.5 x 10^{-6} for structures wider than about 10 km in MU$_{69}$'s equatorial plane (Fig. S4). Any ring around MU$_{69}$ is thus also fainter in forward scattering than Jupiter's main ring (I/F = 4 x 10^{-6} at this phase angle).

New Horizons' Student Dust Detector (SDC) instrument (*44*) detected no signals above the noise threshold within +/- 5 days of the MU$_{69}$ encounter, implying that there were no impacts by dust particles > 1.6 μm in radius, giving a 90% confidence upper limit of 3 x 10^{7} particles km^{-2}. For 10% albedo, this is equivalent to an I/F limit of 3 x 10^{-11}, even more constraining than the optical limit, for particles of this size or larger.

Comparison to Other KBOs, and Possible Captured KBOs

Though most other known CCKBOs are larger than MU$_{69}$, due to discovery biases, it appears typical of CCKBOs using the few other metrics that we can directly compare. As noted by (*1*), MU$_{69}$'s V-band geometric albedo of 0.165 ± 0.01 is typical for CCKBOs (*45*). MU$_{69}$'s phase coefficient, 0.035 magnitudes/degree (*1*), is within the range 0.029 – 0.036 magnitudes/degree found for other small KBOs observed at long range by New Horizons (*13,46*). Rotational lightcurves suggest that up to 25% of larger CCKBOs could be contact binaries like MU$_{69}$ (*11*), though contact binaries appear to be more abundant, up to 50%, in the Plutino population (*47*). Its color is also typical of CCKBOs (*1,3*).

Though many irregular satellites of the giant planets may be captured KBOs, only three have been usefully resolved by spacecraft. Neptune's satellite Triton, diameter 2700 km, is far too large and active to be a useful comparison body to MU$_{69}$. Neptune's smaller irregular satellite Nereid, 170 km in diameter, has a geometric albedo of 0.16 – 0.20, very similar to MU$_{69}$, but is neutral in color (*48*). Saturn's 210 km diameter irregular satellite Phoebe (possibly a captured Kuiper Belt Object (*49*), though perhaps instead a captured C-type asteroid (*50,51*)), is darker (geometric albedo 0.08 (*52*)) and less red (*53*), and has a completely different surface appearance, dominated entirely by impact features (*54*). If Phoebe ever resembled MU$_{69}$, it has been drastically altered by subsequent evolution.

Comparison to Jupiter Family Comets

The class of objects previously explored by spacecraft that are most analogous to MU$_{69}$ in ultimate origin are the Jupiter Family Comets (JFCs). These differ from MU$_{69}$ in three major ways: (i) Provenance: the vast majority of these bodies likely originated in the Kuiper belt, but from a different family of KBOs: the population of "scattered KBOs" which likely originated closer to the sun than MU$_{69}$, and whose orbits are strongly perturbed by gravitational interactions with Neptune (*55*); (ii) Size: the effective spherical diameters of the JFC nuclei explored so far are 3x – 18x smaller than that of MU$_{69}$; (iii) Thermal history: most importantly, JFCs have experienced intense solar heating which has heavily modified their surfaces. By comparing the properties of MU$_{69}$ and JFC nuclei, we can explore the effects of these differences.

The JFC nuclei visited by spacecraft have diverse shapes and surfaces (Fig. 8, Fig S3 and Table S3)). Comets 19P, 67P, and 103P appear to be highly elongated bilobate objects, suggesting the merger of two distinct bodies, as has been proposed for MU$_{69}$ (*1*), though for comets it is also possible that thermal evolution has generated this shape (e.g., *56*). Except for 67P, whose bulk density is 538 ± 1 kg/m^3 (*14*), the densities of the other JFC nuclei discussed here are generally uncertain by a factor of two or more, but all are consistent with ~500 kg/m^3, which imply

average bulk porosities of ~50-80%. MU_{69}'s density is likely greater than 290 kg/m^3 (above), and thus at least consistent with those of JFC nuclei. The rotation period of MU_{69} is comparable to those measured for 67P and 103P and falls well within the range measured for the JFC population (*57*), though JFC comet rotation is known to be affected by their activity.

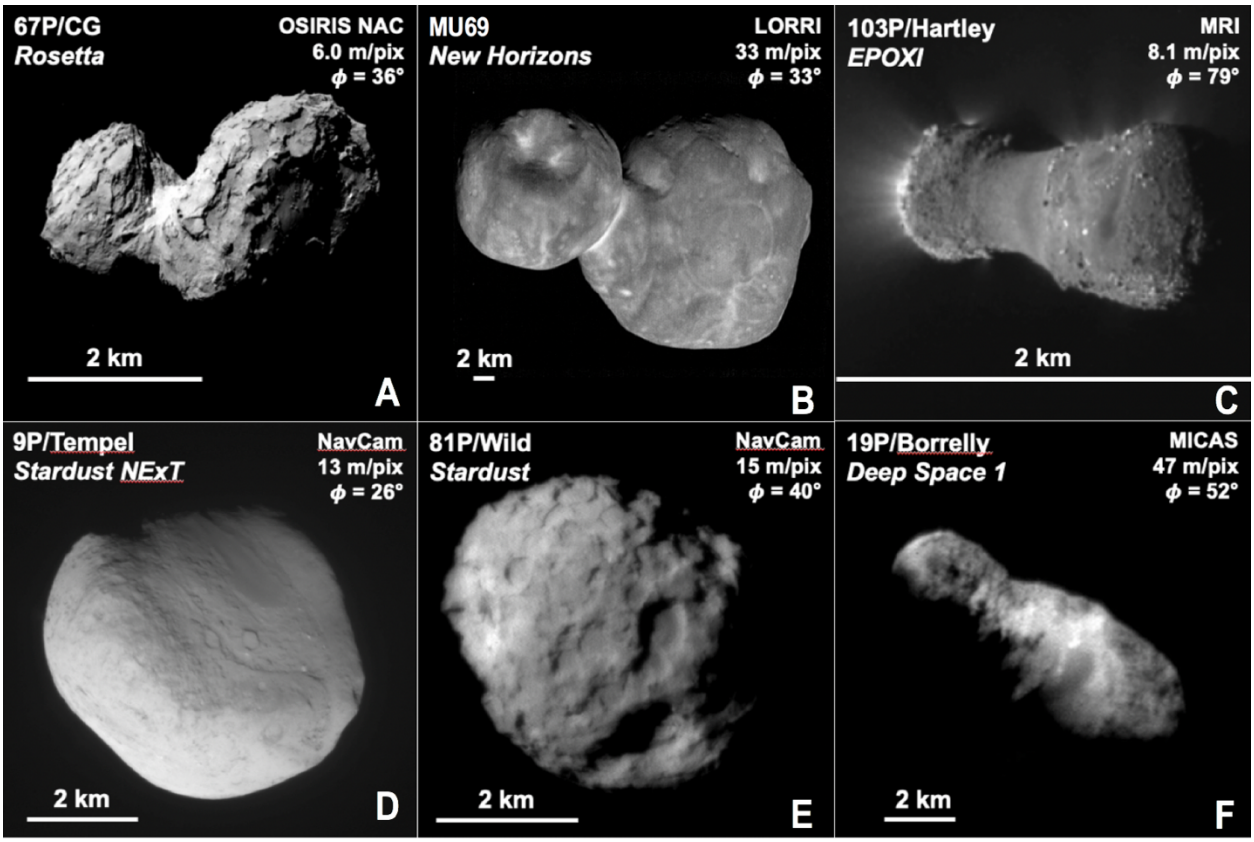

Fig. 8. *Comparison of JFC nuclei and MU_{69}. A: The images of JFC nuclei shown here have phase angles similar to those of the highest resolution image of MU_{69}, except for 103P, which was only observed at much higher phase angles. Images sources are as follows. A: Rosetta (63); B: New Horizons (this paper); C: EPOXI (64); D and E: Stardust (65,66); F: Deep Space 1 (67). Each frame is adjusted so that the body nearly fills it, but the scale bars show the true relative sizes of each body: MU_{69} is much larger than these comets. Figure S3 shows the appearance of these comets at resolutions comparable the MU_{69} image.*

The JFC nuclei discussed here are much darker than MU_{69}, with ~2-3 times smaller geometric albedos (Table S3). If the JFC nuclei once had higher albedos in their nascent state in the Kuiper belt, then the darkening of their surfaces might be associated with cometary activity when the JFCs evolve in the inner solar system. Indeed, most of the surface features on the JFC nuclei have been attributed to cometary activity (e.g., *58,59*). Generally, the surfaces of JFC nuclei can be divided into "smooth" and "rough" (or "mottled") regions, with the rough terrains associated with a preponderance of pits/depressions or mounds/hills (*60,61*). The smooth regions of JFCs are generally brighter than average and are often associated with gravitational lows, suggesting accumulation by small grains that scatter light more efficiently than the average surface, as also proposed for MU_{69} above. However, on comets fallback of grains ejected by sublimation is

likely to be an important contributor to smooth terrains, and this is less likely to be important on MU_{69} where evidence for sublimation erosion is much more limited.

While the gross many-km scale bilobate morphology of MU_{69} is similar to 4 out of the 6 inner system comets resolved to date (Figs. 8, S3), the finer surface texture is not. JFC Comets imaged at the same resolution as MU_{69} by New Horizons show an extreme paucity of impact craters vs MU_{69} (*58*), consistent with inner system comets having highly erosional surfaces, losing ~0.5-1.0 m/revolution with 5-10 yr orbital periods, so that small pits will be removed on timescales of 1000 yrs.. They also show a much rougher surface texture at the 50-100 m scale consistent with sublimation erosion and loss of most of the erosional debris.

Conclusions

The new data from the New Horizons flyby of MU_{69} since (*1*) provide a more complete picture of the physical nature of this extraordinary object. Improved rotational coverage taken on approach shows that while both components of MU_{69} are flattened, the flattening is less extreme than initially inferred, and the two components differ more in volume, with a volume ratio of 1.9 ± 0.5. Stereo topography and improved imaging show that the larger Ultima lobe is very flat on the encounter hemisphere. If Ultima is composed of multiple components which accreted separately, as proposed by (*1*), the topographic signature of the boundaries between the components would be expected to be large initially, if the subunits were mechanically similar to Ultima and Thule at the time of their coming into contact (*16*). The observed flatness of Ultima shows that any such discontinuities have been subdued, and in some cases eliminated entirely. If subsequent deposition subdued the boundaries, post-depositional processes must be invoked to explain why many of the boundaries are still visible as differences in surface texture or as linear albedo features. Alternatively, Ultima may be a monolithic body, and the apparent division into sub-units may be due entirely to secondary processes- it is certainly clear that multiple processes in addition to impacts have reworked the surfaces of both Ultima and Thule after their formation, producing the fissures, small dark hills, and sinuous albedo boundaries seen in the images.

Crater densities on MU_{69} are low, but are consistent with a surface age of > 4 Ga, plausibly dating back to the end of accretion, due to the expected low cratering rates in the Kuiper Belt, even if only craters with the highest confidence of being impact features are included in the counts. Crater size-frequency distribution slopes for < 1 km craters on MU_{69} are poorly constrained, but are at least consistent with the slopes seen for 2 – 15 km craters in the Pluto system (*35*), suggesting that the shallow size-frequency distribution for 0.2 - 2 km diameter KBO impactors found by (*35)* may persist down to even smaller sizes.

MU_{69} is in a fundamentally different category from other studied small bodies. The surfaces of comets are dominated by volatile loss and sublimation erosion driven by the thermal energy inputs from their position in the inner solar system. The surfaces of asteroids are dominated by high-energy impacts. As a result, asteroid surfaces are primarily rubble or impact ejecta. In both cases the dominant energy environment (thermal and impact) is driving the surface morphology. MU_{69}'s surface is probably a consequence of its presence in the cold classical Kuiper belt which is a much more benign energy environment. The very small relative velocities in this dynamical population result in few impacts and very slow impact velocities. Without strong energy inputs either from solar radiation or impacts, the surface of MU_{69} becomes dominated by low level energy inputs from galactic, solar, and micro-meteorite energy sources at slow rates, likely extending to just a few meters depth (*24*). It is this low-energy environment that allows its post-accretionary surface to be preserved.

In all respects that we can currently evaluate, MU_{69} appears to be a typical CCKBO, and that much the information returned from our only close flyby of one of these unique objects can therefore be extended to understand the cold classical belt as a whole. The bi-lobed nature of MU_{69} suggests that contact binaries are common in the Kuiper Belt, and increases the likelihood the bi-lobed nature of many comet nuclei is a primordial feature. We can also expect that surfaces on many or most CCKBOs have been little modified on scales of tens of meters since accretion.

Further implications of the New Horizons findings for the origin of MU_{69} are discussed in (*3*) and *16*).

References and Notes:

1. S. A. Stern., et al. Initial results from the New Horizons exploration of 2014 MU69, a small Kuiper Belt Object. *Science* 364, eaaw9771 (2019).
2. S. B. Porter, M. W. Buie, A. H. Parker and 10 colleagues. High-precision Orbit Fitting and Uncertainty Analysis of (486958) 2014 MU69. Astron. J. 156, 20. (2018).
3. W. M. Grundy et al. Color, Composition, and Thermal Environment of Transneptunian Object (486958) 2014 MU69, Science, submitted (2019).
4. J.-M. Petit et al., The Canada-France Ecliptic Plane Survey - full data release: The orbital structure of the Kuiper belt. Astron. J. 142, 131.1-24 (2011).
5. S. Greenstreet, B. Gladman, W. B. McKinnon, J. J. Kavelaars, K. N. Singer. Crater Density Predictions for New Horizons Flyby Target 2014 MU69. *Astrophys. J.. Lett.*, *872:L5*. (2019) https://doi.org/10.3847/2041-8213/ab01db
6. S. Greenstreet, B. Gladman, W. B. McKinnon. Impact and cratering rates onto Pluto. Icarus 258, 267. (2015).
7. A. F. Cheng, and 15 colleagues. Long-Range Reconnaissance Imager on New Horizons. Space Science Reviews 140, 189. (2008).
8. D. C. Reuter et al. Ralph: A Visible/Infrared Imager for the New Horizons Pluto/Kuiper Belt Mission. Space Science Reviews 140, 129 (2008).
9. S. D. Benecchi et al. The HST lightcurve of (486958) 2014 MU69. Icarus, submitted (2019).
10. M. W. Buie et al. Size and shape constraints of (486958) 2014 MU69 from stellar occultations. Submitted (2019).
11. A. Thirouin, S. S. Sheppard. Light Curves and Rotational Properties of the Pristine Cold Classical Kuiper Belt Objects. The Astronomical Journal 157, 228. (2019).
12. S. B. Porter et al. New Horizons Distant Observations of Cold Classical KBOs. AAS/Division for Planetary Sciences Meeting Abstracts 509.07. (2018).
13. A. J. Verbiscer et al. Phase curves from the Kuiper belt: photometric properties of "distant" KBOs observed by New Horizons. Astron. J., 158, id 123 (2019)
14. F. Preusker et al. The global meter-level shape model of comet 67P/Churyumov-Gerasimenko. Astron. Astrophys. 607, id.L1, (2017).

15. D. J. Scheeres. *Orbital Motion in Strongly Perturbed Environments: Applications to Asteroids, Comet and Planetary Satellite Orbiters*. Springer-Praxis, Chichester. (2012).

16. W. B. McKinnon et al. The solar nebula origin of (486958) 2014 MU69, a primordial contact binary in the Kuiper Belt. Science, submitted (2019).

17. B. Buratti, J. Veverka, J. Voyager photometry of Europa. Icarus 55, 93 (1983).

18. S. Besse, P. Lamy, L. Jorda, S. Marchi, C. Barbieri. Identification and physical properties of craters on Asteroid (2867) Steins. *Icarus*, *221*, 1119-1129 (2012). doi:10.1016/j.icarus.2012.08.008.

19. M. S. Robinson, P. C. Thomas, J. Veverka, S. L. Murchie, B. B. Wilcox. The geology of 433 Eros. *Meteorit. Planet. Sci.*, *37*, 1651-1684 (2002), doi:10.1111/j.1945-5100.2002.tb01157.x.

20. L. Prockter, P. Thomas, M. Robinson, J. Joseph, A. Milne, B. Bussey, et al. Surface expressions of structural features on Eros. *Icarus*, *15*), 75–93 (2002). https://doi.org/10.1006/icar.2001.6770.

21. D. L. Buczkowski, O. S. Barnouin-Jha, L. M. Prockter. 433 Eros lineaments: Global mapping and analysis. *Icarus*, *193*, 39–52 (2008). https://doi.org/10.1016/j.icarus.2007.06.028.

22. S. J. Morrison, P. C. Thomas, M. S. Tiscareno, J. A. Burns, J. Veverka. Grooves on small Saturnian satellites and other objects: Characteristics and significance. *Icarus*, *204*, 262–270. (2009). https://doi.org/10.1016/j.icarus.2009.06.003.

23. T. A. Hurford, E. Asphaug, J. N. Spitale, D. Hemingway, A. R. Rhoden et al. Tidal disruption of Phobos as the cause of surface fractures. *Journal of Geophysical Research: Planets*, *121*, 1054–1065 (2016). https://doi:10.1002/2015JE004943.

24. S. A. Stern. The evolution of comets in the Oort cloud and Kuiper belt. Nature 424, 639 (2003).

25. M. Jutzi, E. Asphaug. The shape and structure of cometary nuclei as a result of low-velocity accretion. Nature 348, 1355-1358 (2015).

26. K. R. Housen, W. J. Sweet, K. A. Holsapple, K.A. Impacts into porous asteroids. *Icarus*, *300*, 72–96 (2018). http://dx.doi.org/10.1016/j.icarus.2017.08.019.

27. S. J. Robbins et al. Measuring impact crater depth throughout the solar system. Meteoritics and Planetary Science 53, 583 (2018).

28. K. A. Holsapple, K. R. Housen, A crater and its ejecta: An interpretation of Deep Impact. Icarus 191, 586–597 (2007). doi: 10.1016/j.icarus.2006.08.035.

29. D. Nesvorný. Dynamical Evolution of the Early Solar System. Annual Review of Astronomy and Astrophysics 56, 137 (2018).

30. S. Sugita et al., The geomorphology, color, and thermal properties of Ryugu: Implications for parent-body processes. *Science* **364**, 252-252 (2019). 10.1126/science.aaw0422.

31. K. J. Walsh et al., Craters, boulders and regolith of (101955) Bennu. *Nature Astron.* **12**, 242–246 (2019). doi: 10.1038/s41561-019-0326-6.

32. D. J. Scheeres et al., The dynamic geophysical environment of (101955) Bennu based on OSIRIS-REx measurements. *Nature Astron.* **3**, 352–361 doi: 10.1038/s41550-019-0721-3 (2019).

33. A. H. Parker, The intrinsic Neptune Trojan orbit distribution: Implications for the primordial disk and planet migration. Icarus 247, 112-125 (2015).

34. S. Mazrouei, R. R. Ghent, W. F. Bottke, A. H. Parker, T. M. Gernon, Earth and Moon impact flux increased at the end of the Paleozoic. Science 363, 253-257 (2019).

35. K. N. Singer, et al. Impact craters on Pluto and Charon indicate a deficit of small Kuiper belt objects. *Science*, *363*, 955-959 (2019).

36. K. S. Noll, W. M. Grundy, D. Nesvorný, A. Thirouin. Transneptunian Binaries (2018). Chapter in *The Trans-Neptunian Solar System*, D. Prialnik, M. A. Barucci, L. Young (eds), Elsevier, in press. (2019).

37. W. R. Johnston, Binary Minor Planets Compilation V2.0. urn:nasa:pds:ast_binary_parameters_compilation::2.0. NASA Planetary Data System, (2018).

38. F. Marchis et al. The Puzzling Mutual Orbit of the Binary Trojan Asteroid (624) Hektor. Astrophys. J. 783, L37 (2014).

39. Descamps, P. et al. Triplicity and physical characteristics of Asteroid (216) Kleopatra. Icarus 211, 1022 (2011).

40. F. Braga-Ribas et al., A ring system detected around the Centaur (10199) Chariklo. Nature 508, 72–75 (2014). doi: 10.1038/nature13155; pmid: 24670644

41. J. L. Ortiz et al., The size, shape, density and ring of the dwarf planet Haumea from a stellar occultation. Nature 550, 219–223 (2017). doi: 10.1038/nature24051; pmid: 29022593.

42. J. L. Ortiz, et al. Possible ring material around centaur (2060) Chiron. Astronomy and Astrophysics 576, A18 (2015).

43. T. R. Lauer et al. The New Horizons and Hubble Space Telescope search for rings, dust, and debris in the Pluto-Charon system. Icarus 301, 155 (2018).

44. M. Horanyi et al. The Student Dust Counter on the New Horizons Mission. Space Science Reviews 140, 387 (2008).

45. P. Lacerda et al., The albedo-color diversity of transneptunian objects. Astrophys. J. 793, L2 (2014). doi: 10.1088/2041-8205/ 793/1/L2

46. A. S. Stern, J. R. Spencer, A. Verbiscer, H. E. Elliot, S. B. Porter. Plans for and initial results from the exploration of the Kuiper Belt by New Horizons. Chapter in *The Trans-Neptunian Solar System*, D. Prialnik, M. A. Barucci, L. Young (eds), Elsevier, in press. (2019).

47. A. Thirouin, S. S. Sheppard. The Plutino Population: An Abundance of Contact Binaries. The Astronomical Journal 155, 248 (2018).

48. P. Thomas, J. Veverka, P. Helfenstein. Voyager observations of Nereid. Journal of Geophysical Research 96, 19253 (1991).

49. T. V. Johnson, J. Lunine. Saturn's moon Phoebe as a captured body from the outer Solar System. *Nature* **435**, 69-71 (2005).

50. W. K. Hartmann, A satellite-asteroid mystery and a possible early flux of scattered C-class asteroids. Icarus 71, 57-68 (1987). doi: 10.1016/0019-1035(87)90162-X

51. J. Castillo-Rogez, P. Vernazza, K. Walsh 2019. Geophysical evidence that Saturn's Moon Phoebe originated from a C-type asteroid reservoir. Monthly Notices of the Royal Astronomical Society 486, 538 (2019).

52. D. P. Simonelli, J. Kay, D. Adinolfi, J. Veverka, P. C. Thomas, P. Helfenstein. Phoebe: Albedo Map and Photometric Properties. Icarus 138, 249 (1999).

53. B. J. Buratti, M. D. Hicks, K. A. Tryka, M. S. Sittig, R. L. Newburn. High-resolution 0.33–0.92 mm spectra of Iapetus, Hyperion, Phoebe, Rhea, Dione, and D-type asteroids: How are they related? Icarus155, 375–381 (2002).

54. C. C. Porco et al. Cassini Imaging Science: Initial Results on Phoebe and Iapetus. Science 307, 1237 (2005)

55. M. Duncan, H. Levison, L. Dones, L. Dynamical evolution of ecliptic comets. In Comets II, M. C. Festou, H. U. Keller, and H. A. Weaver (eds.), University of Arizona Press, Tucson 193 (2004).

56. D. E. Vavilov, S. Eggl, Y. D. Medvedev, P. B. Zatitskiy. Shape evolution of cometary nuclei via anisotropic mass loss. Astron. Astrophys. 622, L5 (2019).

57. R. Kokotanekova et al. Rotation of cometary nuclei: new light curves and an update of the ensemble properties of Jupiter-family comets. Monthly Notices of the Royal Astronomical Society 471, 2974 (2017).

58. J. Sunshine, N. Thomas, M. R. El-Maarry, T. L. Farnham. Evidence for geologic processes on comets, J. Geophys. Res. Planets, 121 (2016). doi:10.1002/2016JE005119.

59. M. R. El-Maarry et al. Surface changes on comet 67P/Churyumov-Gerasimenko suggest a more active past. Science 355, 1392–1395 (2017). DOI: 10.1126/science.aak9384.

60. P. C. Thomas et al. Shape, density, and geology of the nucleus of Comet 103P/Hartley 2. Icarus 222, 550-558 (2013).

61. D. T. Britt et al. The morphology and surface processes of Comet 19/P Borrelly. Icarus 167, 45-53 (2004).

62. H. J. Melosh. Impact cratering : a geologic process. New York : Oxford University Press ; Oxford : Clarendon Press (1989).

63. H. Sierks et al. On the nucleus structure and activity of comet 67P/Churyumov-Gerasimenko. Science 347, aaa1044 (2015).

64. M. F. A'Hearn et al. EPOXI at Comet Hartley 2. Science 332, 1396 (2011).

65. J. Veverka et al. Return to Comet Tempel 1: Overview of Stardust-NExT results. Icarus 222, 424-435 (2013).

66. D. E. Brownlee et al. Surface of Young Jupiter Family Comet 81 P/Wild 2: View from the Stardust Spacecraft. Science 304, 1764-1769 (2004).

67. L. A. Soderblom et al. Observations of Comet 19P/Borrelly by the Miniature Integrated Camera and Spectrometer Aboard Deep Space 1. Science 296, 1087-1091 (2002).

68. R. A. Beyer, O. Alexandrov, S. McMichael. The Ames Stereo Pipeline: NASA's Open Source Software for Deriving and Processing Terrain Data. Earth Space Sci. 5, 537-548 (2018). http://doi.org/10.1029/2018ea000409

69. R. A. Beyer, O. Alexandrov S. McMichael. NeoGeographyToolkit/StereoPipeline: NASA Ames Stereo Pipeline 2.6.1 (Version v2.6.1). Zenodo (2018), http://doi.org/10.5281/zenodo.1345235

70. Y. Chen, G. Medioni. Object modelling by registration of multiple range images. Image and Vision Computing 10, 145-155. (1992). https://doi.org/10.1016/0262-8856(92)90066-C

71. P. J. Besi, N.D. McKay. A method for registration of 3-D shapes. IEEE Transactions on Pattern Analysis and Machine Intelligence 14, 239 – 256 (1992). https://doi.org/10.1109/34.121791

72. J. A. Skinner, A. E. Huff, C. M. Fortezzo, T. A. Gaither, T. M. Hare, M. A. Hunter, Planetary Geologic Mapping Protocol-2018. USGS, Flagstaff, AZ (2018).

73. K. N. Singer, W. B. McKinnon, L. T. Nowicki. Secondary craters from large impacts on Europa and Ganymede: Ejecta size–velocity distributions on icy worlds, and the scaling of ejected blocks. Icarus 226**,** 865-884 (2013).

74. E. B. Bierhaus et al. Secondary craters and ejecta across the solar system: Populations and effects on impact-crater-based chronologies. Meteoritics and Planetary Science 53, 638 (2018).

75. J. M. Moore et al. Great Expectations: Plans and predictions for New Horizons encounter with Kuiper Belt Object 2014 MU69 ("Ultima Thule"). *Geophys. Res. Lett.*, 45 (2018). https://doi.org/10.1029/2018GL078996.

76. J.-Y. Li et al. Photometric properties of the nucleus of Comet 103P/Hartley 2. Icarus 222, 559-570 (2013).

77. S. Fornasier et al. Spectrophotometric properties of the nucleus of comet 67P/Churyumov-Gerasimenko from the OSIRIS instrument onboard the ROSETTA spacecraft. Astronomy and Astrophysics 583, A30 (2015).

78. P. L. Lamy, I. Toth, Y. R. Fernandez, H. A. Weaver. The sizes, shapes, albedos, and colors of cometary nuclei, in *Comets II*, M. C. Festou, H. U. Keller, and H. A. Weaver (eds.), University of Arizona Press, Tucson, 223-264 (2004).

79. B. J. Buratti, M. D. Hicks, L. A. Soderblom, D. Britt, J. Oberst, J. K. Hillier 2004. Deep Space 1 photometry of the nucleus of Comet 19P/Borrelly. Icarus 167, 16-29 (2004).

Acknowledgments: We thank all who contributed to the success of the New Horizons flyby of 2014 MU_{69}, and in particular the National Astronomical Observatory of Japan's Subaru Telescope, the Carnegie Observatory's Magellan Telescopes, the Canada-France-Hawaii Telescope, the NASA Hubble Space Telescope, the Harvard-Smithsonian Center for Astrophysics, the Massachusetts Institute of Technology, Northern Arizona University, the University of Hawaii, the Hertzberg Institute for Astrophysics, and NASA, for their support of the search campaign that led to its discovery. We also are indebted to the Hubble Space Telescope and the European Space Agency's Gaia mission for their key roles in the precise orbit

determination required to enable the successful flyby. **Funding:** Supported by NASA's New Horizons project via contracts NASW-02008 and NAS5- 97271/TaskOrder30. Also supported by the National Research Council of Canada (J.J.K.). **Author contributions:** J.R.S., J.M.M., H.A.W., K.N.S., A.J.V., R.A.B., J.T.K., T.R.L., S.B.P., O.L.W., B.J.B., H.B.T., O.M.U., W.B.M. and J.D.H. were responsible for drafting the manuscript and figures. S.A.S. is the principal investigator of the New Horizons mission and reviewed this manuscript. All other authors participated in mission planning, initial discovery and tracking of 2014 MU_{69}, science data reduction or analysis, and/or provided inputs and critique to this manuscript. **Competing interests:** We declare no competing interests. **Data and materials availability**: All images, spacecraft data, and the shape model used in this paper are available at TBD [resolve before publication]. Additional fully calibrated New Horizons MU_{69} data and higher-order data products will be released by the NASA Planetary Data System at https://pds-smallbodies.astro.umd.edu/data_sb/missions/newhorizons/index.shtml in a series of stages in 2020 and 2021, owing to the time required to fully downlink and calibrate the dataset.

List of Supplementary Materials

Supplemental Text

Figures S1-S4

Tables S1-S3

External Database S1

Movie S1

Shape Models S1, S2

References (*68* - *79*)

Science
AAAS

Supplementary Materials for

Title: The Geology and Geophysics of Kuiper Belt Object (486958) 2014 MU69

J.R. Spencer, S.A. Stern, J.M Moore, H.A. Weaver, K.N. Singer, C.B Olkin, A.J. Verbiscer, W.B. McKinnon, J.Wm. Parker, R.A. Beyer, J.T. Keane, T.R. Lauer, S.B. Porter, O.L. White, B.J. Buratti, M.R. El-Maarry, C.M. Lisse, A.H. Parker, H.B. Throop, S.J. Robbins, O.M. Umurhan, R.P. Binzel, D.T. Britt, M.W. Buie, A.F. Cheng, D.P. Cruikshank, H.A. Elliott, G.R. Gladstone, W.M. Grundy, M.E. Hill, M. Horanyi, D.E. Jennings, J.J. Kavelaars, I.R. Linscott, D.J. McComas, R.L. McNutt Jr., S. Protopapa, D.C. Reuter, P.M. Schenk, M.R. Showalter, L.A. Young, A.M. Zangari, A.Y. Abedin, C.B. Beddingfield, S.D. Benecchi, E. Bernardoni, C.J. Bierson, D. Borncamp, V.J. Bray, A.L. Chaikin, R.D. Dhingra, C. Fuentes, T. Fuse, P.L Gay, S.D.J. Gwyn, D.P. Hamilton, J.D. Hofgartner, M.J. Holman, A.D. Howard, C.J.A. Howett, H. Karoji, D.E. Kaufmann, M. Kinczyk, B.H. May, M. Mountain, M. Pätzold, J.M. Petit, M.R. Piquette, I.N. Reid, H.J. Reitsema, K.D. Runyon, S.S. Sheppard, J.A. Stansberry, T. Stryk, P. Tanga, D.J. Tholen, D.E. Trilling, L.H. Wasserman

Correspondence to: spencer@boulder.swri.edu

Revised August 27th 2019

This PDF file includes:

Supplementary Text
Figs. S1 to S4
Tables S1 to S3
Captions for Data Table S1, Movie S1, and shape models S1, S2

Other Supplementary Materials for this manuscript include the following:

Data Table S1 (*data_table_s1.csv*)
Movie S1 (*movie_s1.mp4*)
Shape models S1, S2 (*shape_model_s1.obj, shape_model_s2.obj*)

Supplementary Text

Construction of Stereo Models

Three sets of LORRI images, called CA04, CA05, and CA06 (Table S1) provide the highest-resolution stereo coverage. Each set consists of multiple overlapping images taken during a simultaneous scan of the Ralph instrument, which are registered, stacked, and deconvolved to produce the final images used for analysis. The CA05 / CA06 pair has the best nominal resolution and a good stereo convergence angle (17°). However, the CA04 / CA06 pair (Fig. 1A) provides better stereo because, in addition to a slightly larger convergence angle (almost 20°), CA04 has a much longer effective exposure time (thus better SNR), and also lower smear, than CA05 (Table S1). We used the Ames Stereo Pipeline (*68*,*69*) on the stacked, deconvolved products from the CA04 & CA06 observations to derive a stereographic terrain model of the surface of MU_{69}. An iterative closest point algorithm (*70*,*71*) was used to rigidly rotate and translate the stereo model surface to match the -Z facing surface of the global shape model, though the required rotation was minimal, < 0.5º.

Planetary Geomorphological Mapping as Applied to MU_{69}

Constructing a planetary geomorphological map derived solely from images acquired above the study area involves defining and characterizing discrete material units based primarily on the surface morphology, texture, albedo, and color as seen at the pixel scale, which are physical attributes that are related to the geologic processes that produced them. Along with visible structural features, the distributions of these units are then mapped to identify the relative roles of different geological processes that shape planetary surfaces. We have followed standard US Geological Survey mapping protocol (*72*) when creating our geomorphological map of MU_{69} (Fig. 1C), although applying the principles of mapping to it can be challenging, primarily because our highest resolution observations of the target (138 to 33 m/pixel) were only obtained at relatively low phase angles (12.9° to 32.5°). Outside of a narrow strip proximal to the terminator, this hinders assessment of topography at a scale of hundreds of meters based on surface shading. In addition, the consistently low phase of the approach imaging generates uncertainty regarding how much of the observed surface heterogeneity across MU_{69} is due to intrinsic geological variation, or is a consequence of variable illumination of a limited range of geomorphological units. In addition, we emphasize that we have created a geomorphological, rather than a geological map, i.e. the units that we have defined for MU_{69} have been inferred from what appear to be distinct physiographic components of Ultima and Thule, but the map is not intended to rigorously convey stratigraphic relations between units. Stratigraphic organization of the units would require application of the rules of superposition and crosscutting, which we do not consider to be feasible given the limitations of available data and inherent ambiguities associated with its interpretation. Instead, the map is intended to reduce the complexity of MU_{69}'s surface into comprehensible proportions that are more amenable to the development of hypotheses for the formation and evolution of MU_{69}.

On Ultima, which shows less overall albedo variation but more limb topographic amplitude than Thule, the boundaries of the individual sub-units that compose this lobe have been defined based largely on topographic expression as presented in the LORRI CA06 33 m/pixel imaging, and as revealed in stereo imaging (e.g. comparing LORRI CA04 and CA06 in Fig. 1A). High solar incidence angles proximal to the terminator make troughs and scarps separating subunits visible here (including those separating units *tb*, *tc*, and *sm*). In contrast, the boundary of unit *tg*,

located on the limb of Ultima, is inferred not based on shading due to topography, but due to it being ringed by bright material (unit *bm*), which we interpret to be loosely-consolidated material that has collected in depressions across MU_{69}, most notably at the neck connecting Ultima and Thule. Stereo imaging is crucial to the identification of unit *tf* as a separate unit, as its apparent position can be seen to move relative to unit *te* between LORRI CA04 and CA06. While albedo variation across Ultima is low relative to Thule, some units are distinguished by their albedo characteristics, such as units *ta*, *tc*, and *td*, which appear lighter-toned than the neighboring units of *te*, *th*, and *sm*, despite these latter units being illuminated at lower solar incidence angles. Unit *tg* is distinguished from unit *te* not only by the partial stretch of bright material that exists between them, but also by the observation that unit *tg* displays a surface pattern characterized by albedo contrasts on a scale of hundreds of meters, whereas unit *te* appears dark and homogeneous at this scale by comparison. The boundary between units *sm* and *th* is located in the center of the face of Ultima, far from the terminator and the limb, and there is no apparent topographic discontinuity associated with it. Instead, a tentative contact has been defined based on the differing textures presented by these units (unit *th* shows greater albedo contrast than unit *sm*) as well as the presence of a portion of the bright annulus that separates them, although we have identified locations where some darker elements of unit *th*, apparently hills, extend across the annulus. Inasmuch as we perceive there are distinct physiographic units on Ultima, for the sake of hypothesis testing in this study, we treat them as individual geomorphological units, even if future investigations decide that they are in fact all topographic expressions of the same unit.

On Thule, units on the sunlit side are defined primarily according to the different albedos and planforms they present; any topographic signatures associated with them are much less apparent when compared with those of subunits under similar lighting conditions on Ultima, which is at least in part due to the smaller scales of the Thule units. Thule's limb topography, however, does indicate a break in slope that corresponds to the stretch of dark material (unit *dm*) that separates units *mm* and *rm*, and suggests that unit *mm* occupies a local high, whereas unit *rm* occupies a local low. This topographic discontinuity is an important factor in the decision to map these areas as separate units: whereas unit *rm* displays a pitted surface and unit *mm* does not, the two units cannot be mapped separately based on this criterion alone, as we cannot rule out that variable illumination has played a role in contributing to their different appearances.

These examples demonstrate how every aspect of available imaging (in particular stereo parallax, surface shading at low and high solar incidence angles, and limb topography) must be exploited and carefully considered in order to identify discrete geomorphological units in this data-limited scenario.

Expected Impact Crater Morphologies

Despite the low impact velocities, we expect most impacts on MU_{69} to form craters similar to those seen elsewhere in the solar system. Crater morphology varies with the impactor and target characteristics. The low and high velocity tails of the impact velocity distribution reach down to a few m s^{-1} and as high as a few km s^{-1}, but the most common primary impact speed onto MU_{69}, ~300 m s^{-1} (*5*), is relatively slow, typical of secondary cratering velocities on the surfaces of both icy and rocky bodies closer to the sun (*73,74*). These impacts often form craters with similar morphological characteristics to primary craters, although secondary craters are often shallower than the same size primary impact, and may be elongated in the direction radial to the primary crater. We are not suggesting any craters on MU_{69} are secondary craters, but secondary craters elsewhere show that 300 m s^{-1} impacts are capable of creating craters on the surface of MU_{69}.

The formation of a crater on a slope or modification by later geologic processes (such as mass wasting or a subsequent fault near the crater) may also alter the crater's appearance.

The R Value Measure of Crater Densities

The R value plotted on Fig. 6B of the main paper is constructed from a differential power law size-frequency distribution of crater diameters ($dN/dD \propto D^q$) that is normalized by a D^{-3} distribution, where N is the crater spatial density and D is the diameter. The power law exponent (q) is commonly referred to as the distribution log-log slope. In this visualization, a crater size-frequency distribution with a slope of -3 will be a horizontal line, allowing differences from the commonly seen D^{-3} distribution to be easily seen.

Crater Identification and Classification

Feature size measurements were carried out on the original CA06 LORRI image. Since no projection was used, the crater sizes were measured in pixels and converted to approximate sizes using the pixel scale of 33 m px^{-1}. Care was taken to measure the most representative diameter of a feature (e.g., to avoid foreshortening where possible). The size for the crater Maryland is an average of 6 chords. Some features have more distinct boundaries than others. For interpreting crater diameters given here, we recommend a diameter uncertainty of 2 pixels or 20% of the crater diameter, whichever is larger for a given features (i.e., for features above 10 pixels, or ~330 m, we recommend using 20%).

Data Table S1 includes the crater sizes and subgroup designations for each feature considered for crater analysis and shown in Fig. 6A in the main body of the paper. Some features were determined to have a low likelihood of being either fresh or modified craters, and thus are not included in any subgroup plotted in fig. 6B. The descriptions for each subset are below and additional information is in Table S2.

- The UT_High Confidence subgroup includes only features 0.34 km (~10 pixels) or larger in diameter, only fairly circular features, and features with the topography expected of craters. This does include a few more subtle features but they are all features closer to the terminator.
- The UT_Medium Confidence subgroup includes smaller and/or less circular features. It includes 4 features less than 0.34 km in diameter, from ~0.23 – 0.27 km across.
- The UT_Low Confidence subgroup includes features that are depressions or bright spots but considerably less circular, and features in a chain that may be associated with a tectonic feature (at a subunit boundary). It includes 6 features less than 0.34 km in diameter, from ~0.19 – 0.28 km across.
- The U_Bright subgroup, designed to give an approximation of a maximum density, includes: all UT_High, Medium, and Low features larger than 0.27 km (8 pixels), that are bright, circular or sub-circular features on the sunward half of Ultima only (right of the solid line in Fig. 6A).
- The U_Pits subgroup, designed to give an approximation of a maximum density, includes: all UT_High, Medium, and Low features larger than 0.27 km, both circular and less circular and also include few features in a chain, that are on the anti-sunward half of Ultima only (left of the solid line in Fig. 6A).

- The U_Term subgroup, designed to give an approximation of a maximum density, includes: all UT_High, Medium, and Low features larger than 0.27 km, both circular and sub-circular features, and a few features that may be in a chain, in the near-terminator region left of the dashed line on Fig. 6A.

Details of Satellite Searches

Searches conducted to assess flyby hazards from 42 to 19 days before the flyby covered the entire Hill sphere (~40,000 km radius assuming an MU_{69} density of 500 kg m^{-3}) with a range of total exposure times up to 1 hour. Later 2x2 and 4x4 frame image mosaics, taken from 3.3 days to 6 hours before the flyby with 2.6 – 12 minute total exposures, covered smaller regions with greater sensitivity. Each search consisted of 2 – 3 mosaics taken 0.6 – 2.0 hours apart, in order to identify satellites by their motion relative to the dense Milky Way star background. These deep searches overexposed MU_{69} and thus had limited sensitivity very close to it, so close approach images exposed for MU_{69}'s surface were used to search for satellites with very small orbital radii. Sensitivity limits were established by implanting synthetic objects into the original images.

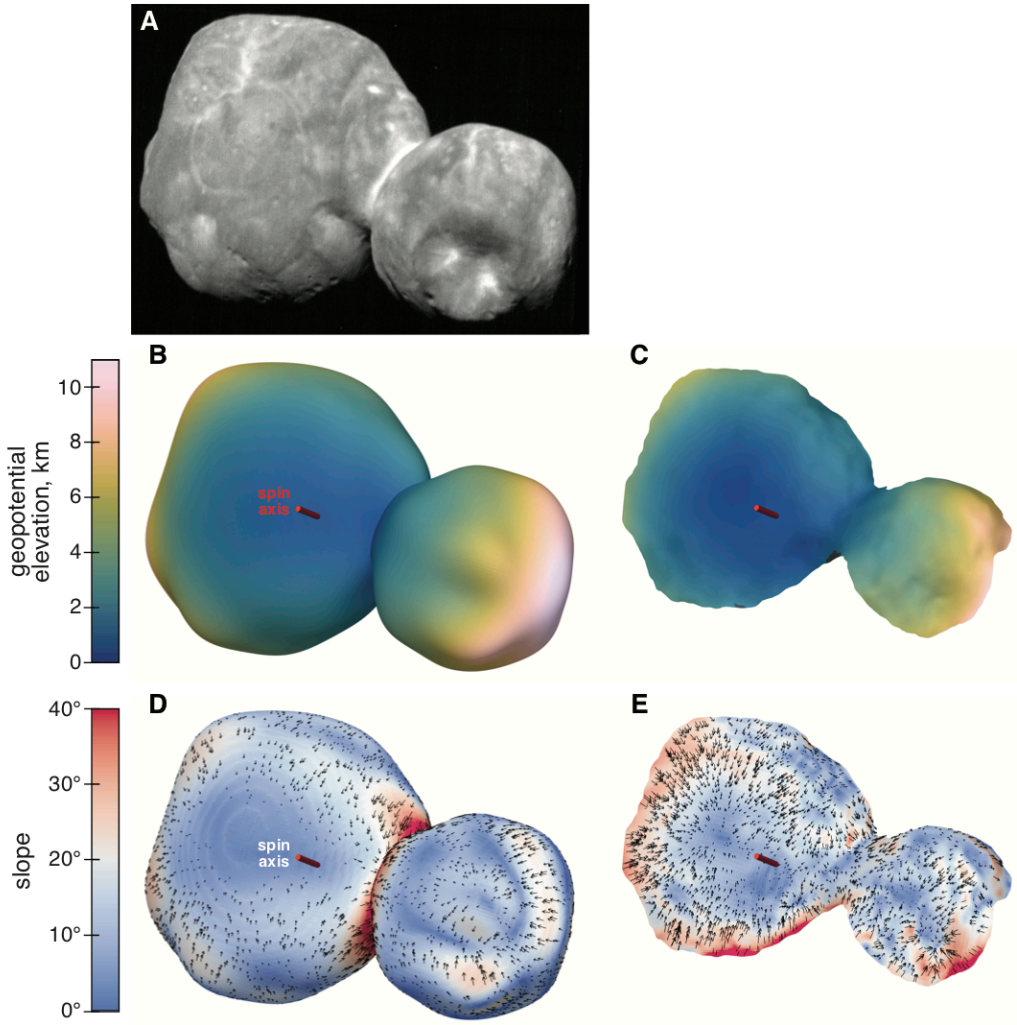

Fig. S1. Slopes and Gravity of MU$_{69}$. *CA06 image of MU$_{69}$ (A) compared to illustrations of gravitational parameters seen from the same geometry. B and C: Geopotential elevation for the global shape model (B) and stereo model (C). D and E: Slopes computed from the global shape model (D) and stereo model (E). Color gives slope magnitude, and arrows give the slope direction.*

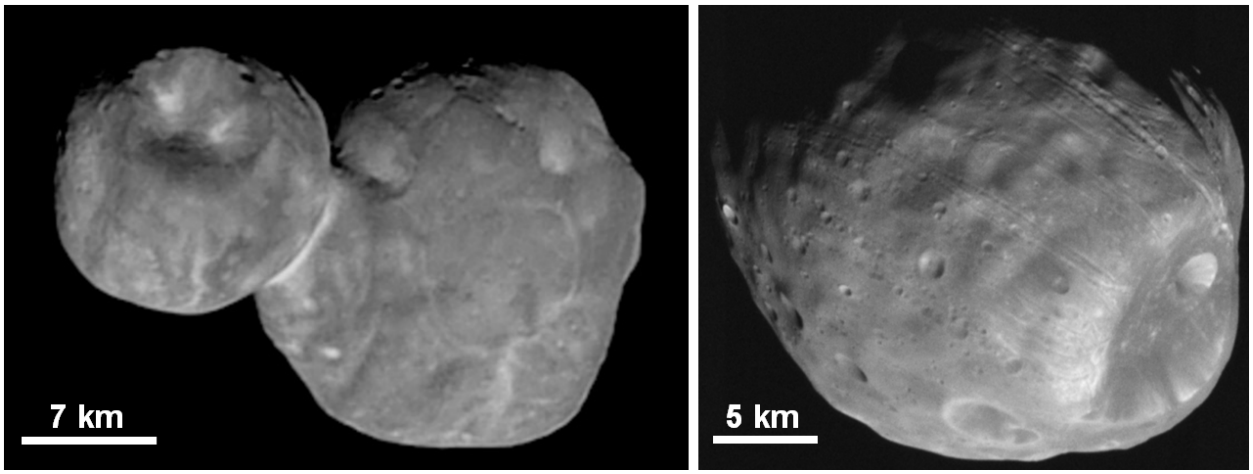

Fig. S2. *Craters on MU_{69} compared to those on the Martian moon Phobos. An image of the Martian moon Phobos (right, diameter = 22.5 km) from the Mars Reconnaissance Orbiter obtained at a similar but slightly lower phase angle (26.4°) to our highest resolution MU_{69} image (CA06, left) at 32° phase (75). The image of Phobos has been processed to match the pixel scale, smear, camera point-spread-function, SNR, and deconvolution of our highest resolution LORRI images of MU_{69}. Many more unambiguous craters can be seen across the surface of Phobos than on MU_{69}.*

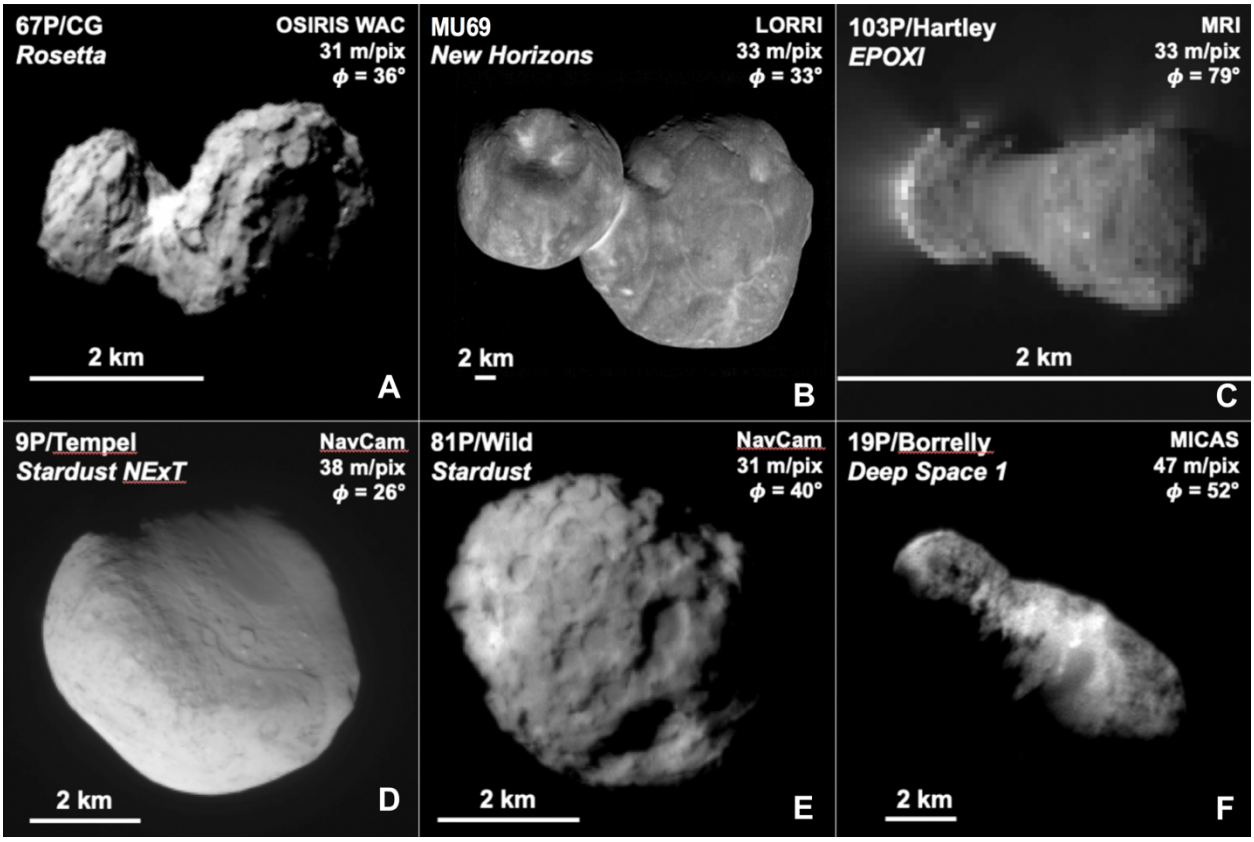

Fig. S3. *Images of JFC nuclei and MU_{69} at comparable pixel scale. A: The images of JFC nuclei shown here have spatial resolutions and phase angles similar to those of the highest resolution image of MU_{69}, except for 103P, which was only observed at much higher phase angles. Images sources are as follows. A: Rosetta (63); B: New Horizons (this paper); C: EPOXI (64); D and E: Stardust (65,66); F: Deep Space 1 (67). Each frame is adjusted so that the body nearly fills it, but the scale bars show the true relative sizes of each body. For higher-resolution image comparisons, see Figure 8 in the main body of the paper.*

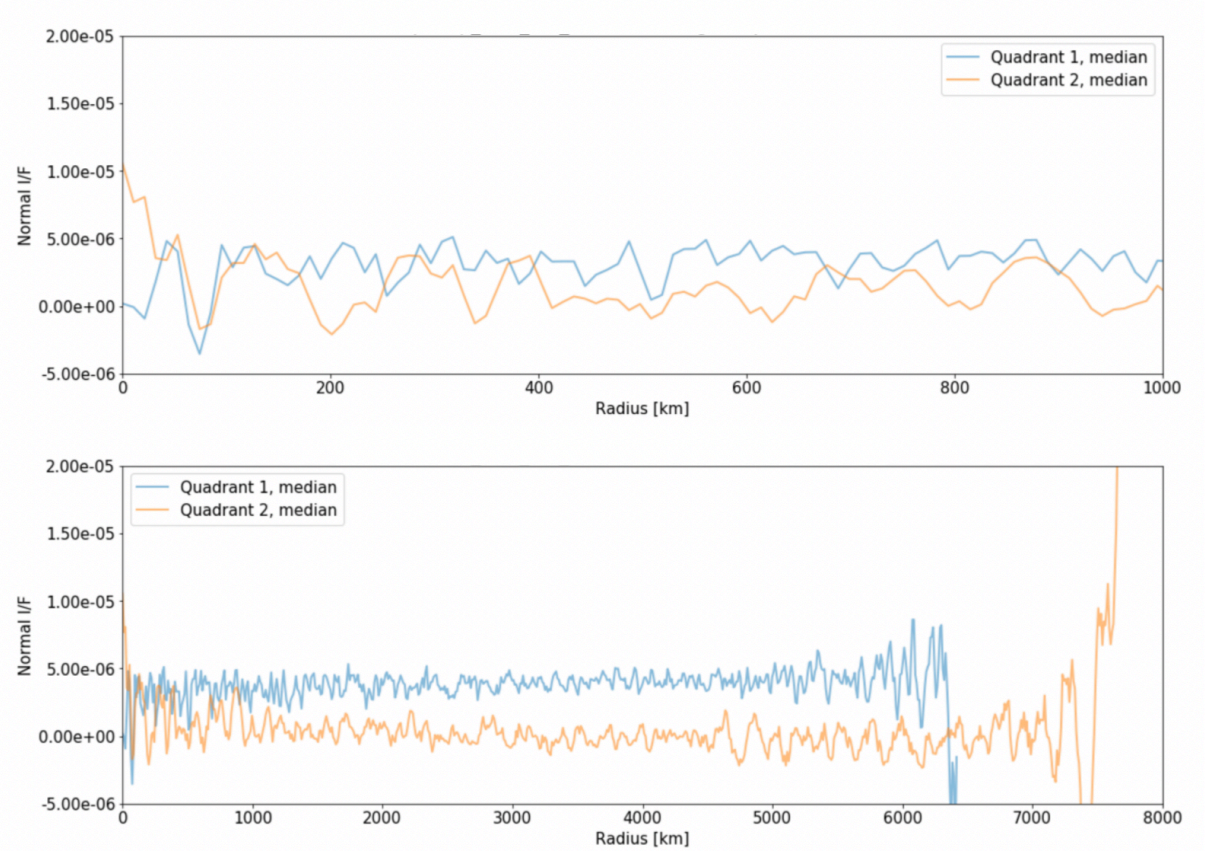

Fig. S4. *Non-Detection of forward-scattering rings around MU_{69}. Radial profiles of the sky brightness, in units of I/F, as a function of distance from MU_{69} in its equatorial plane, from MVIC images taken 1.7 – 2.3 hours after closest approach at a phase-angle of 168°. The upper panel shows the innermost region, and the lower panel shows the entire profile. The blue and orange curves were derived from different quadrants of the image: the vertical offset between them is an artifact. Profiles are binned to a spatial resolution of 10.6 km. No rings or dust structures were seen, with an upper limit I/F of ~1.5 x 10^{-6} for structures wider than about 10 km.*

Image set name	Mode	Mid-Time, mins. after C/A	Range, km	Phase, degrees	Resolution, km /pixel	Smear, pixels	Single-Frame Exposure time, sec	Number of Co-added Frames	Combined Exposure time, sec
CA01	LORRI 1x1	-70.6	61,214	11.8	0.304	0.6	0.150	43	6.45
CA02	LORRI 1x1	-49.1	42,663	12.0	0.212	4.0	0.025	6	0.15
CA04	LORRI 1x1	-31.9	27,850	12.9	0.138	0.4	0.100	25	2.50
CA05	LORRI 1x1	-18.8	16,680	15.7	0.083	4.0	0.025	6	0.15
CA06	LORRI 1x1	-6.5	6,634	32.5	0.033	4.0	0.025	6	0.15
CA07	LORRI 4x4	9.4	8,834	152.4	0.175	8.1	0.200	6	1.20

Table S1*. Close Approach LORRI Images*

Subgroup	Location	Number of features*	Diameter range (km)*	Surface area used (km^2)	Area description
UT_High	U & T	10	0.34–7.16	700	Entire visible surface of MU_{69}: Area is ½ of the global shape model surface area
UT_Medium	U & T	17	0.24–0.64		
UT_Low	U & T	16	0.19–0.68		
U_Bright	U Only	10	0.27–0.62	230	Sunward half of Ultima: Area is ½ of Ultima's visible surface area
U_Pits	U Only	14	0.27–0.77	230	Anti-sunward half of Ultima: Area is ½ of Ultima's visible surface area
U_Term	U Only	8	0.27–0.77	90	Measured from the shape model for the selected area

Table S2. *Feature subgroups for crater analysis. Data Table S1 includes the full list of craters and sizes with classification information.*

Object ID	Ellipsoid Axes (km)	Spherical Diameter (km)	Density (kg m^3)	Rotational Period (hr)	Geometric Albedo
MU_{69}	35 x 20 x 10	16.8	>290	15.9	0.165
9P/Tempel	7.6 x 4.9 x 4.6	5.6	200-600	~41	0.056
19P/Borrelly	8.0 x 3.2 x 3.2	4.3	290-830	~25	0.065
67P/Churyumov-Gerasimenko	4.3 x 2.6 x 2.1	2.9	533 ± 6	~12	0.058
81P/Wild	5.5 x 4.0 x 3.3	4.2	-	-	0.059
103P/Hartley	2.2 x 0.5 x 0.5	0.92	200-400	~18	0.045

Table S3*. Sizes, densities, rotational periods, and geometric albedos of MU_{69} and cometary nuclei. The object IDs are listed in the first column. The second column refers to the best fit ellipsoid dimensions, even though the actual shape may differ significantly from an ellipsoid. The effective spherical diameters, calculated from the best fit ellipsoidal dimensions in column 2, are presented in the third column and provide perhaps the best single number for the "size" of the object. The density for 67P is exceedingly well determined (14) and lies roughly in the middle of the ranges estimated JFC nuclei. Due to the jetting force from cometary outgassing, the rotational periods of JFC nuclei change with time, so only approximate current values are listed for them. The geometric albedos are for a wavelength of 550 nm (V-band) and are taken from (76,77), sometimes with small corrections to transform from R-band (650 nm) to V-band using the typical value for JFC colors as reported in (78). The variation of reflectance across the surfaces of the JFC nuclei and Ultima Thule are comparable (±15-20% variation about the global mean value), except for 19P, which shows a variation about twice that of the other objects, apparently associated with two different types of terrains (79).*

Data Table S1 (Separate file: filename data_table_s1.csv). This table lists the identification numbers for the craters and pits shown in Fig. 6A, their diameters, and the confidence classes and geographical groupings assigned to each.

Movie S1 (Separate file: filename *movie_s1.mp4*). Animation of the global shape model of MU_{69}

rotating about its true spin axis (red arrow), highlighting the encounter hemisphere. The model is colored to show geopotential altitude, and is obliquely illuminated.

Shape Model S1 (separate file: filename *shape_model_s1.obj*). Stereo shape model of the surface of MU_{69} that was visible to New Horizons near closest approach, derived from the CA04 and CA06 LORRI images.

Shape Model S2 (separate file: filename *shape_model_s2.obj*). Global shape model of MU_{69}, obtained from the complete set of LORRI images.